

Effective power-law dependence of Lyapunov exponents on the central mass in galaxies

N. Delis,^{1,2} C. Efthymiopoulos^{2★} and C. Kalapotharakos^{3,4}

¹Department of Physics, University of Athens, Panepistimiopolis, 115 21 Athens, Greece

²Research Center for Astronomy and Applied Mathematics, Academy of Athens, Soranou Efessiou 4, 115 27 Athens, Greece

³University of Maryland, College Park (UMDCP/CRESST), College Park, MD 20742, USA

⁴Astrophysics Science Division, NASA/Goddard Space Flight Center, Greenbelt, MD 20771, USA

Accepted 2015 January 12. Received 2015 January 9; in original form 2014 March 5

ABSTRACT

Using both numerical and analytical approaches, we demonstrate the existence of an effective power-law relation $L \propto m^p$ between the mean Lyapunov exponent L of stellar orbits chaotically scattered by a supermassive black hole (BH) in the centre of a galaxy and the mass parameter m , i.e. ratio of the mass of the BH over the mass of the galaxy. The exponent p is found numerically to obtain values in the range $p \approx 0.3$ – 0.5 . We propose a theoretical interpretation of these exponents, based on estimates of local ‘stretching numbers’, i.e. local Lyapunov exponents at successive transits of the orbits through the BH’s sphere of influence. We thus predict $p = 2/3 - q$ with $q \approx 0.1$ – 0.2 . Our basic model refers to elliptical galaxy models with a central core. However, we find numerically that an effective power-law scaling of L with m holds also in models with central cusp, beyond a mass scale up to which chaos is dominated by the influence of the cusp itself. We finally show numerically that an analogous law exists also in disc galaxies with rotating bars. In the latter case, chaotic scattering by the BH affects mainly populations of thick tube-like orbits surrounding some low-order branches of the x_1 family of periodic orbits, as well as its bifurcations at low-order resonances, mainly the inner Lindblad resonance and the 4/1 resonance. Implications of the correlations between L and m to determining the rate of secular evolution of galaxies are discussed.

Key words: chaos – galaxies: kinematics and dynamics – galaxies: structure.

1 INTRODUCTION

There is by now overwhelming evidence that black holes (BHs) with masses ranging from 10^6 to $10^{10} M_\odot$ (see review Ferrarese & Ford 2005) exist in the centre of most galaxies: Kormendy et al. (1995, 1997, 1998), Gebhardt et al. (1996, 2000), Faber et al. (1997), van der Marel, de Zeeuw & Rix (1997), Gültekin et al. (2009a,b), Kormendy & Ho (2013), McConell & Ma (2013). The presence of a supermassive BH leads to a number of consequences for dynamics, whose study has been a subject of extended research in the last three decades (indicative references closely related to our present work are Gerhard & Binney 1985; Merritt & Fridman 1996; Merritt & Valluri 1996; Fridman & Merritt 1997; Kandrup & Sideris 2002; Kalapotharakos, Voglis & Contopoulos 2004; Kalapotharakos & Voglis 2005; see Merritt (1999) or Merritt (2013) for complete reviews of the subject.)

Inter alia, the growth of a central BH provides a mechanism driving *secular evolution* in galaxies. The creation of secularly evolving models by the insertion of a central mass is ubiq-

uitous in N -body simulations of non-rotating elliptical galaxies (Merritt & Quinlan 1998; Holley-Bockelmann et al. 2001, 2002; Contopoulos, Voglis & Kalapotharakos 2002; Jesseit, Naab & Burkert 2005; Kalapotharakos & Voglis 2005; Muzzio, Carpintero & Wachlin 2005; Muzzio 2006; Kalapotharakos 2008; Valluri et al. 2010; Vasiliev & Athanassoula 2012). The secular evolution causes two main effects: i) the density profile becomes more cuspy in the centre (Young 1977, 1980; Holley-Bockelmann et al. 2002), and ii) the galaxy becomes more spherical in the centre and more axisymmetric in the outer parts (Merritt & Quinlan 1998; Kalapotharakos et al. 2004; Kalapotharakos & Voglis 2005). On the other hand, the growth of BHs in disc galaxies slowly disrupts the bars by changing the stability properties of many orbits that support the bar (Pfenniger 1984; Pfenniger & de Zeeuw 1989; Hasan, Pfenniger & Norman 1993; Norman, Sellwood & Hasan 1996; Shen & Sellwood 2004; see review Debattista 2006).

In the case of elliptical galaxies, a physical interpretation of why, after the insertion of a central mass, secular evolution favours particular end states was provided in Kalapotharakos et al. (2004) and Kalapotharakos & Voglis (2005) (see also Efthymiopoulos, Voglis & Kalapotharakos 2007; Kalapotharakos 2008). This is based on closely examining the orbital dynamics of those particles whose

★ E-mail: cefthim@academyofathens.gr

orbits are directly affected by the central mass. The main scenario of the secular evolution process presented in these works can be summarized as follows: at a first stage, the insertion (or gradual ‘turning on’) of the central mass results in a conversion of the majority of box orbits into chaotic orbits (Gerhard & Binney 1985). Following the evolution of the system by N -body simulations, it is found that the newly formed chaotic orbits start inducing a gradual change in the distribution of matter, i.e. the shape of the system, which becomes more spherical given that the distribution of chaotic orbits is more isotropic. The slow change in shape, in turn, causes an adiabatic change in the potential, thus affecting the *phase space structure*, in particular at energies for which the phase space was initially (before the insertion of the central mass) occupied mainly by box orbits passing arbitrarily close to the centre. The main change of the phase space structure regards the volume increase of the domain corresponding to regular short axis tube (SAT) orbits (see Binney & Tremaine 2008 for definition). As the volume of the SAT domain increases, some chaotic orbits are adiabatically captured inside the boundary of the SAT domain (Kalapotharakos et al. 2004). This capture then induces an additional change in the form of the system, enhancing the conversion of chaotic orbits into SAT orbits, etc. This cyclic process maintains secular evolution up to a point where the population of chaotic orbits decreases substantially. The systems evolved by this mechanism are closer to oblate. Furthermore, in the final stages the percentage of chaotic orbits becomes smaller even than the one in the original systems, before the insertion of the central mass.

It should be noted that the degree up to which the transformation of a system from triaxial to axisymmetric proceeds depends on how many box orbits are transformed to chaotically scattered orbits due to the central mass. For example, in Holley-Bockelmann et al. (2002) the initial percentage of outer box orbits is such that an adiabatic introduction of the central mass does not destroy triaxiality in the outer parts of their galaxy simulation models. Also, Valluri et al. (2010) examined how stochastic (or ‘non-reversible’) can the whole process of secular evolution be characterized, by considering the secular evolution of dark matter haloes in various models of central mass concentrations. While their findings reconfirm the picture of (non-reversible) stochastic evolution in the case of a point-like central mass concentration (e.g. a BH), they find that there is also a different, i.e. ‘regular’ (or reversible) type of evolution taking place in systems in which the central mass is spatially distributed (e.g. a galactic disc or bulge embedded in a triaxial halo).

Hereafter, we focus on the mechanism of secular evolution induced by the chaotic scattering of centrophilic orbits. In order to quantify the rate of secular evolution induced by the above mechanism, Kalapotharakos (2008) introduced a novel quantity, measurable in N -body simulations, called the *effective chaotic momentum*:

$$\mathcal{L} = \frac{\Delta N_w}{N_{\text{total}}} L_w. \quad (1)$$

In equation (1), L_w is the mean value of the *Lyapunov characteristic number* (LCN) of a subensemble of chaotic orbits in the system after the insertion of the central mass. This is defined by the orbits belonging to a percentage window ± 0.3 around the characteristic value where the distribution $P(\log L_j)$ of the logarithms of the Lyapunov exponents L_j of all the particles in chaotic orbits presents its global maximum. Considering a percentage window is necessary since, as we will see also below, the distribution $P(\log L_j)$ is two-peaked, while the secular evolution is caused mainly by orbits forming the higher of the two peaks of the distribution. As a rule, these are centrophilic orbits passing arbitrarily closely to the

central mass. On the other hand, ΔN_w is the total mass inside the same window, while N_{total} is the total mass of the N -body system considered.

The use of the effective chaotic momentum \mathcal{L} allows one to quantify several phenomena related to the rate of secular evolution. A remarkable result is that there appears to be a global (i.e. the same in all simulations) threshold value \mathcal{L}_{th} such that as a system undergoes secular evolution, with a time-varying value of $\mathcal{L}(t)$, the evolution becomes inefficient over a Hubble time when $\mathcal{L}(t)$ falls below \mathcal{L}_{th} (Kalapotharakos 2008).

From the two factors in the definition of \mathcal{L} (equation 1), the percentage of chaotic orbits $\Delta N_w/N_{\text{total}}$ depends on the specific system studied, i.e. on the initial distribution function that determines the initial conditions of the simulation. However, as noted in Kalapotharakos et al. (2004) and Kalapotharakos (2008), the distribution of Lyapunov exponents, and in particular the value of L_w is found numerically to be not very sensitive to the choice of initial distribution function in the simulations. Thus, simulations representing systems with different profiles and triaxiality were found to exhibit different percentages of chaotic orbits, but similar levels of L_w , the latter found, instead, to be correlated with the *value of the mass ratio* of the central mass over the mass of the hosting system. Hereafter, this ratio is simply referred to as the ‘central mass parameter’ m . These findings indicate that, from the two factors entering the computation of the rate of secular evolution via the ‘effective chaotic momentum’, one (percentage $\Delta N_w/N_{\text{total}}$ of chaotic centrophilic orbits) depends on the self-consistent distribution function of the system considered, while the other (mean Lyapunov exponent L_w) depends strongly only on the value of the mass parameter m .

In this paper we focus on this latter dependence, and seek to model its dynamical origin. We note that a dependence of the mean Lyapunov exponent L of the centrophilic orbits on m is a result derived also in studies using fixed potentials (e.g. Gerhard & Binney 1985; Merritt & Valluri 1996; Kandrup & Sideris 2002). In Kalapotharakos (2008), on the other hand, this dependence was explicitly determined by the orbital data of the particles in N -body simulations yielding the value of L_w which is a good measure of L . A remarkably good *power-law dependence* was found, namely

$$L \propto m^p, \quad p \approx 0.5. \quad (2)$$

The proximity of p to 0.5 was also found in models of simple galactic potentials (Kalapotharakos 2008). As shown in Section 2, somewhat smaller values, around $p \approx 0.3$, are deduced by a careful a posteriori analysis of the numerical results presented in Merritt & Valluri (1996) and in Kandrup & Sideris (2002).

In this paper we first reconfirm numerically the power law (2) in further fixed-potential computations. Then, we develop a theoretical modelling allowing us to interpret the origin of this power law. We also justify why the exponent p obtains values in the observed range. In particular, our theory yields an exponent $p = 2/3 - q$, where $q \sim 0.1$ – 0.2 .

Our theoretical modelling stems from considering the dynamics of chaotic centrophilic orbits which undergo ‘transits’, i.e. they spend part of their time inside and another part outside the so-called sphere of influence of the central mass (Gerhard & Binney 1985). One may note here that transiting is a necessary condition for chaos, since orbits lying entirely within the sphere of influence (i.e. the so-called pyramids – Merritt & Vasiliev 2011) obey three quasi-integrals of motion which are deformations of the Keplerian integrals derived using perturbation theory (here, the perturbation consists of the triaxial galactic potential, which perturbs the otherwise Keplerian dynamics very close to the BH; see

Merritt & Vasiliev 2011). On reverse, as shown below, for transiting orbits one can determine the so-called *stretching number* (i.e. local Lyapunov number) yielding the local rate of deviation of two orbits with nearby initial conditions across one transit. The Lyapunov exponent, modelled as the sum of many such stretching numbers, turns then to be positive, i.e. the orbits are chaotic. We provide various types of evidence for the validity of this approximation, which allows us to predict a (positive) mean value for the Lyapunov exponent as a function of the central mass parameter m . It is remarkable, in this respect, that during a transit the motion can be characterized as nearly Keplerian, while far from transits the motion is box-like and obeys three approximate integrals. Thus, both ‘piecewise’ motions can be analysed by nearly-integrable approximations. Nevertheless, their union yields chaos.

In our basic modelling we use a simple galactic model with a harmonic core. This ensures a priori the presence of many box orbits before the insertion of the BH. However, it is well known that realistic galactic models present power-law central density cusps $\rho(r) \propto r^{-\gamma}$ (Ferrarese et al. 1994; Lauer et al. 1995; see review in Binney & Merrifield 1998, section 4.3.1). Central cusps are characterized as ‘weak’ if $\gamma < 1$ or ‘strong’ if $\gamma > 1$, with the central force tending to zero or to infinity, respectively. It is well known (e.g., Merritt & Valluri 1996) that the central cusps are themselves an important source of chaos for centrophilic orbits. Thus, they significantly affect the value of L even without the presence of a central BH. We will show, however, by numerical tests, that the presence of the central cusp introduces a critical mass parameter scale m_c , depending on the value of γ , such that, for $m > m_c$ the chaotic scattering is dominated by the BH, while for $m < m_c$ it is dominated by the central cusp. As shown in Section 4, we then essentially recover an effective power law $L \propto m^p$ for $m > m_c$. Finally, we present numerical evidence that an effective power law of the same form applies in rotating disc-barred galaxies with central BHs. In this case, the relevant mass parameter m corresponds to the ratio of the mass of the BH over the total mass of the bar. In summary, although our theoretical interpretation for the origin of the effective law $L \propto m^p$ is strictly valid in a quite simplified (and rather unrealistic) galactic model, our numerical evidence is that such a law appears generically in models of increasing complexity (and astrophysical interest).

The structure of this paper is as follows: Section 2 presents further numerical results about the empirical relation $L \propto m^p$, using a simple galactic-type potential to which we add the potential of the central mass. These results are used in order to probe numerically some aspects of subsequent modelling. Our theoretical modelling itself is presented in Section 3. Section 4 presents numerical results in models with central cusps and discusses the extent and limits of validity of previous results on the correlation between L and m in such models. Section 5 deals with the $L \propto m^p$ relation in barred disc galaxy models, discussing both its applicability and origin, despite the non-existence, in such systems, of box-like orbits. Section 6 summarizes the main conclusions of the present study.

2 NUMERICAL RESULTS

2.1 Hamiltonian model and numerical integrations

At first we study the relation between L and m in a simple Hamiltonian model that captures the main features of motion near the centre of an elliptical galaxy with non-singular central force field, to which we add a Keplerian term corresponding to the central mass.

The Hamiltonian is

$$H(x, y, z, p_x, p_y, p_z) = \frac{p_x^2}{2} + \frac{p_y^2}{2} + \frac{p_z^2}{2} + V(x, y, z), \quad (3)$$

where $V = V(x, y, z)$ is the gravitational potential:

$$V(x, y, z) = \frac{1}{2}\omega_1^2 x^2 + \frac{1}{2}\omega_2^2 y^2 + \frac{1}{2}\omega_3^2 z^2 + \varepsilon(xz + xy + y^2)^2 - m/\sqrt{r^2 + d^2}. \quad (4)$$

The variables (x, y, z) are Cartesian position coordinates, (p_x, p_y, p_z) their conjugate momenta, and $r = \sqrt{x^2 + y^2 + z^2}$. The softening parameter d was added in the Keplerian potential in order to avoid large numerical errors when the orbits pass very close to the centre. We selected a set of incommensurable frequencies $\omega_1 = 1, \omega_2 = \sqrt{2}, \omega_3 = \sqrt{3}$ so as to avoid dealing with resonant orbits satisfying some low-order commensurability. The anharmonicity parameter ε was given values between 0.01 and 0.5. Various tests of the robustness of our results against ε are reported below. We also note that the quartic potential term was chosen so as to represent a generic form without particular symmetries, while in galaxies with one or more planes of symmetry the potential presents a corresponding even symmetry.

The gravitational potential (4) corresponds to a galaxy model with a harmonic core. The far more realistic case in which a central cusp is present is examined in detail in Section 4 below. Here, the choice of the potential ensures a priori the existence of many regular box orbits, when $m = 0$, which are transformed to chaotically scattered orbits when $m \neq 0$. In the model (4), the force grows linearly with distance from the centre, while the force from the central mass falls as an inverse square law. The two forces become similar in magnitude at distances comparable to the radius (Gerhard & Binney 1985):

$$r_m = m^{1/3} r_c. \quad (5)$$

The sphere $r = r_m$ is called sphere of influence of the central mass. The parameter r_c is of order unity in units in which the frequencies $\omega_x, \omega_y, \omega_z$ are of order unity (as in equation 3). Then, for the total mass of the galaxy one also has $M \sim r_c^3 = O(1)$. The periods of orbits reaching apocentric positions $r_a \gg r_m$ are of order $T \sim 2\pi$.

The equations of motion resulting from the Hamiltonian (3) are

$$\begin{aligned} \dot{x} &= p_x \\ \dot{y} &= p_y \\ \dot{z} &= p_z \\ \dot{p}_x &= -\omega_1^2 x - 2\varepsilon(xz + xy + y^2)(z + y) + mx/(r^2 + d^2)^{3/2} \\ \dot{p}_y &= -\omega_2^2 y - 2\varepsilon(xz + xy + y^2)(x + 2y) + my/(r^2 + d^2)^{3/2} \\ \dot{p}_z &= -\omega_3^2 z - 2\varepsilon(xz + xy + y^2)x + mz/(r^2 + d^2)^{3/2}. \end{aligned} \quad (6)$$

In Lyapunov exponent computations we also make use of the variational equations:

$$\begin{aligned} \delta\dot{x} &= \delta p_x \\ \delta\dot{y} &= \delta p_y \\ \delta\dot{z} &= \delta p_z \\ \delta\dot{p}_x &= -\frac{\partial^2 V}{\partial x^2} \delta x - \frac{\partial^2 V}{\partial x \partial y} \delta y - \frac{\partial^2 V}{\partial x \partial z} \delta z \\ \delta\dot{p}_y &= -\frac{\partial^2 V}{\partial y \partial x} \delta x - \frac{\partial^2 V}{\partial y^2} \delta y - \frac{\partial^2 V}{\partial y \partial z} \delta z \\ \delta\dot{p}_z &= -\frac{\partial^2 V}{\partial z \partial x} \delta x - \frac{\partial^2 V}{\partial z \partial y} \delta y - \frac{\partial^2 V}{\partial z^2} \delta z. \end{aligned} \quad (7)$$

In numerical computations we solve together the equations (6) and (7). We use a seventh–eighth order Runge–Kutta method with fixed time step $\Delta t = 10^{-4}$. For a choice of softening $d = 10^{-3}$, this time step ensures that energy is conserved to within an error between 10^{-12} and 10^{-10} for all orbits.

The LCN is defined through the relation

$$\text{LCN} = \lim_{t \rightarrow \infty} \frac{1}{t} \ln(\xi(t)/\xi(0)), \quad (8)$$

where

$$\xi(t) = \sqrt{\delta x(t)^2 + \delta y(t)^2 + \delta z(t)^2 + \delta p_x(t)^2 + \delta p_y(t)^2 + \delta p_z(t)^2}.$$

In practical computations we make use of the finite-time LCN:

$$\chi(t) = \frac{1}{t} \ln(\xi(t)/\xi(0)). \quad (9)$$

We made computations for ensembles of $n = 200$ orbits for the mass parameter values $m = 10^{-5}, 3 \times 10^{-5}, 10^{-4}, 3 \times 10^{-4}, 10^{-3}, 3 \times 10^{-3}, 10^{-2}$, as well as the values of the anharmonicity parameter $\varepsilon = 0.01, 0.1$, and 0.5 . The initial conditions of each ensemble are chosen as follows. For each initial condition, we choose first randomly a value of the energy in the range $0 \leq E \leq 0.2$, with uniform distribution. Then, we produce an orbit of zero initial angular momentum, by setting $p_x = p_y = p_z = 0$ and by solving for r the equation $E = V(r, \theta, \phi)$, where (r, θ, ϕ) are spherical coordinates corresponding to the Cartesian point (x, y, z) , and $\cos \theta, \phi$ are chosen randomly with a uniform distribution in the intervals $[-1, 1]$ and $[0, 2\pi)$, respectively. The selected range of energies represents motions with apocentric distances of order $r \approx r_c$. These are all centrophilic orbits with a zero mean value of either component of the angular momentum.

2.2 Results

Fig. 1 shows the time evolution of the finite-time Lyapunov exponent $\chi(t)$ for the whole ensemble of orbits in one of the numerical experiments where $m = 10^{-3}$ and $\varepsilon = 0.1$. The integration was up to the time $t = 10^5$. Almost all orbits in this ensemble are chaotic, as their finite-time Lyapunov exponents are stabilized to non-zero values. Only a small subset of orbits exhibit a value of $\chi(t)$ that keeps

falling even at the time $t = 10^5$, following the law $\chi(t) \sim 1/t$. This subset defines regular orbits. The detailed time behaviour of $\log \chi(t)$ for a typical chaotic orbit is shown in Fig. 1(b). A general remark is that for the entire set of parameter values used in our experiments, the large majority of orbits in our ensembles turn to be chaotic. The minimum percentage of chaotic orbits (67 per cent) is observed in the experiment with the minimum values of m and ε , i.e. $m = 10^{-5}$ and $\varepsilon = 0.01$. The classification of orbits as ordered or chaotic is based on a ‘Fast Lyapunov Indicator’ criterion (Froeschlé, Lega & Gonczi 1997), namely on whether the length $\xi(t)$ of the deviation vector is smaller, or larger, respectively, than a threshold value set equal to $\xi_{\text{th}}(t) = 100t$. Fig. 2 shows the distribution of the quantity $\log \chi(t)$ for three different time snapshots ($t = 10^3, 10^4, 10^5$) for the ensembles of orbits in the experiments with central mass values $m = 10^{-4}, 10^{-3}$, and 10^{-2} . In all cases we can see that the distribution $\log \chi(t)$ exhibits a main peak corresponding to the chaotic orbits, which is displaced to higher values of $\log \chi(t)$ as the central mass m increases. On the other hand, for the mass values $m = 10^{-4}$ and 10^{-3} there appears a secondary peak in the distribution of $\log \chi(t)$, that corresponds to the small subset of regular orbits. The secondary peak is displaced to the left, as the quantity $\log \chi(t)$ for regular orbits decreases in time as $-\log t$. For the largest central mass values ($m = 10^{-2}$), however, we observe no secondary peak, i.e. all the orbits turn to be chaotic. Fig. 3 shows the main result. From the histograms of Fig. 2, the mean value $L = \bar{\chi}(t)$ is extracted and plotted against m at the snapshots $t = 10^3, 10^4$, and 10^5 for all the numerical experiments. The straight lines in the same plots (in logarithmic scale) represent power-law fittings of the relation between L and m . The best-fitting exponents in different plots range in values between $p \simeq 0.35$ and $\simeq 0.5$. We also note a tendency towards smaller values for smaller t . However, the bigger values are more representative of the true exponent, since they appear at times closer to the limit when $\chi(t)$ tends to its limiting value for chaotic orbits, i.e. the LCN. If $l = \lim_{t \rightarrow \infty} \chi(t)$ denotes the LCN limit, it is well known (see e.g. Kalapotharakos & Voglis 2005) that the generic behaviour of $\chi(t)$ is to fall like t^{-1} up to a time $t_1 \approx t^{-1}$. The time t_1 is called ‘Lyapunov time’, and represents a saturation time beyond which the curve $\chi(t)$ starts stabilizing towards the limiting value l . The temporal change of $\chi(t)$ for times $t < t_1$ is reflected in the histograms of Fig. 2. We

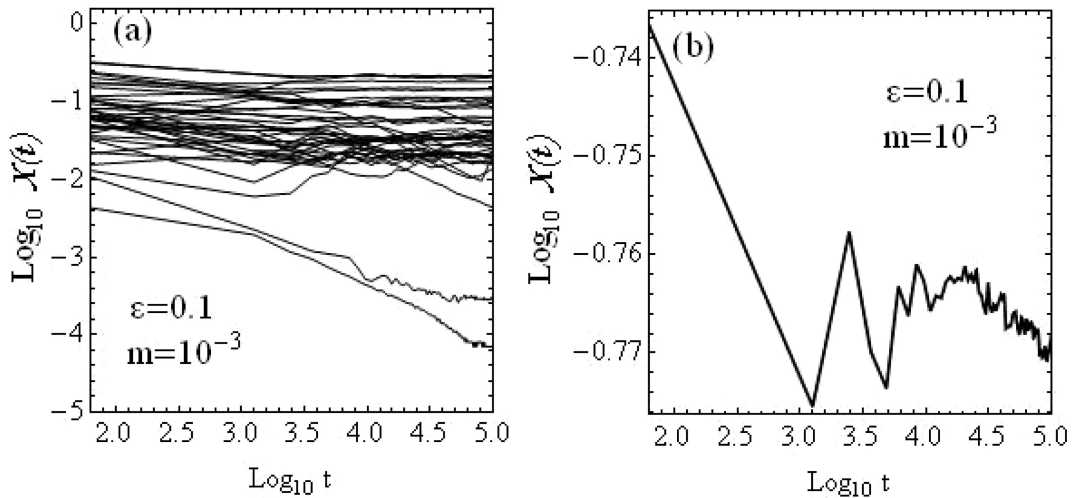


Figure 1. (a) Time evolution of finite Lyapunov numbers for the ensemble of orbits in the case $m = 10^{-3}$, $\varepsilon = 0.1$. (b) The detailed form of the curve $\chi(t)$ for one chaotic orbit (initial conditions $x = 0.064$, $y = -0.0625$, $z = -0.123$, $v_x = 0.064$, $v_y = 0.028$, $v_z = -0.06$). After the time $t = 10^4$ the variations of $\chi(t)$ are less than 2 per cent.

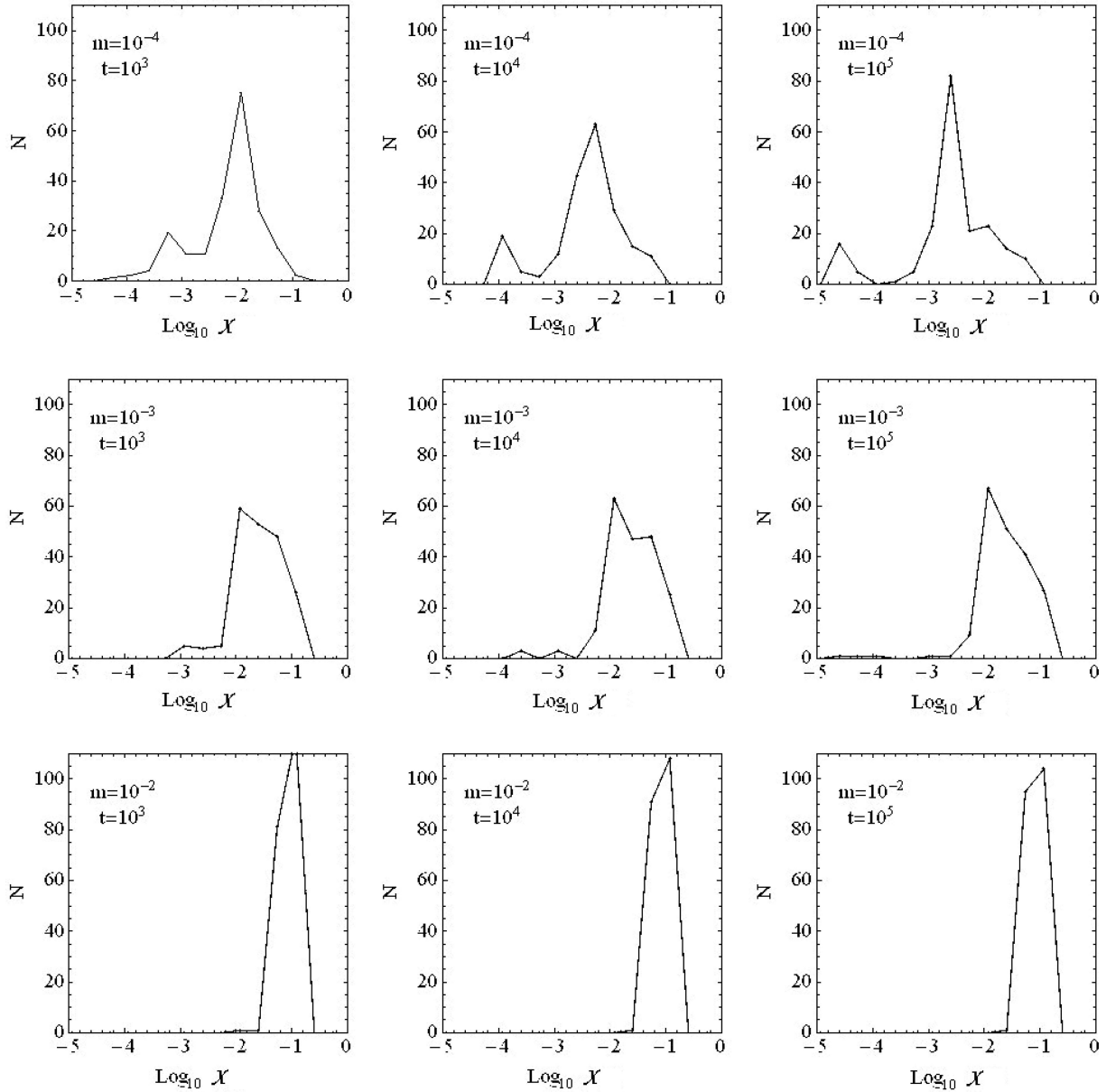


Figure 2. The distributions $P(\log \chi(t))$ for the particles in our ensembles. Every line of histograms corresponds to a different central mass parameter ($m = 10^{-4}, 10^{-3}, 10^{-2}$) whereas every column to a different time snapshot ($t = 10^5, 10^4, 10^3$). The histograms are shown for $\varepsilon = 0.1$.

can observe that, along a fixed panel row (i.e. fixed m , integration time increasing from left to right), the right wing of the histogram is shifted in general to the left as t increases. The shift is more conspicuous in the uppermost panel row (small m), in which the orbits have, in general, smaller values of the LCN, and hence, larger values of their saturation times t_1 . On the other hand, in the lowermost panel row ($m = 10^{-2}$, i.e. large), the saturation time is small ($t_1 < 10^3$ for nearly all orbits). Hence, the histogram $N(\chi)$ remains practically invariant beyond the time $t = 10^3$, as shown in the three panels of the same row.

The difference in the saturation times between small and large m has, as a consequence, that in each *column* of Fig. 3 (same parameters but increasing t), the value of L for all m presents some shift downwards as t increases. The shift is important for small values of m , while it is nearly negligible for large values of m (for which

the orbits reach their saturation times t_1 already before $t = 10^3$). Hence, the effective logarithmic slope p increases as t increases. Nevertheless, the tendency of p to increase with time is only temporary, since p is stabilized after all the orbits have reached their saturation times. This happens around $t = 10^5$. Another remark is that the dependence of the exponent p on the anharmonicity parameter ε appears to be weak. This fact confirms that the main source of the chaotic behaviour of the orbits is the scattering by the central mass, while non-linear effects due to the quartic terms in the potential are of small importance. This agrees with findings in (Kandrup & Sideris 2002). It should be noted, in this respect, that a power-law relation $L \sim m^p$ can be extracted by an a posteriori analysis of data in independent published works (Merritt & Valluri 1996; Kandrup & Sideris 2002). In particular, Kandrup & Sideris (2002) computed finite-time Lyapunov characteristic

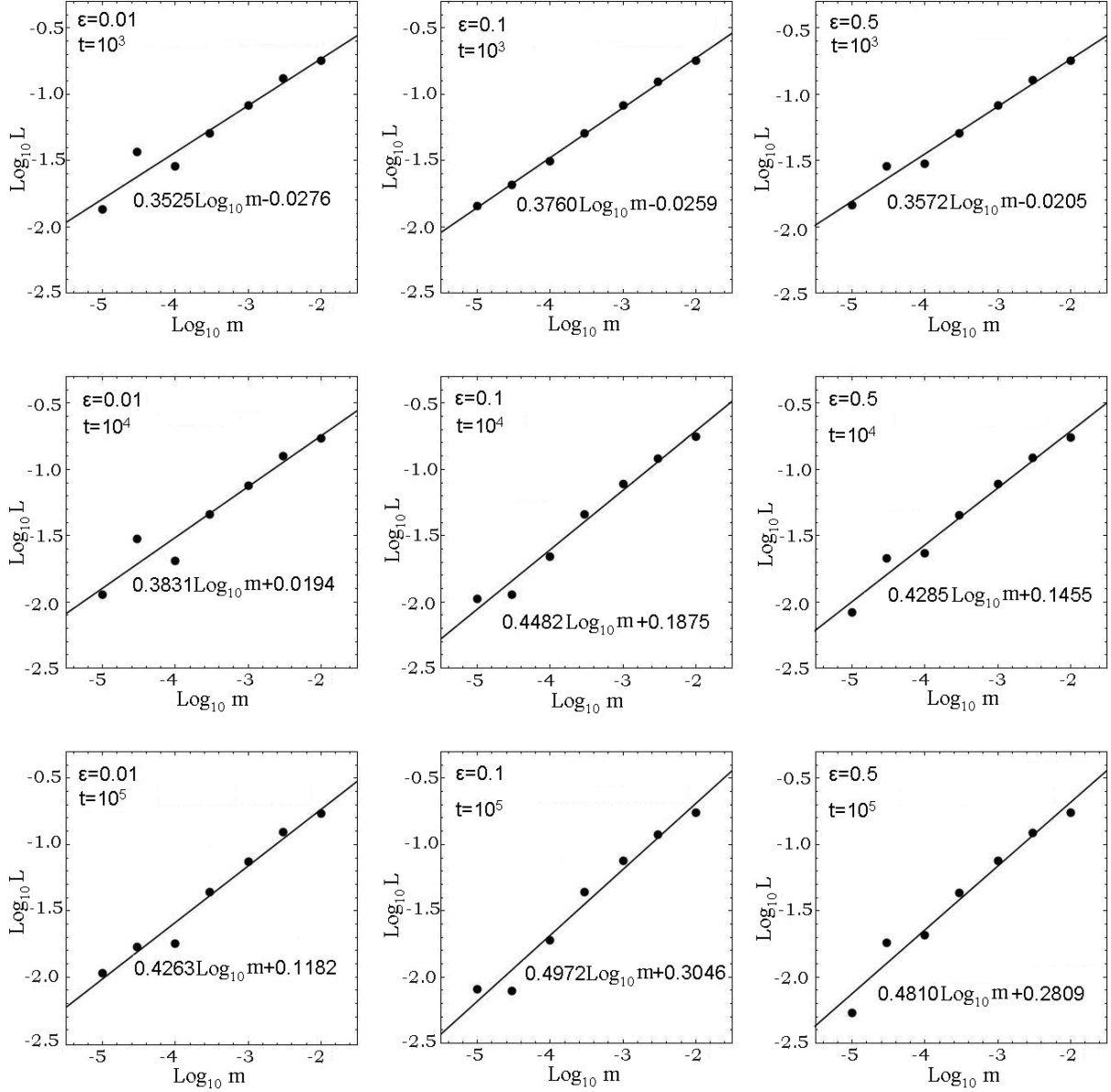


Figure 3. The $L = \overline{\chi(t)}$ versus m relation in logarithmic scale for all our experiments, with parameters as indicated in the panels.

exponents in a potential representing the lowest expansion terms of a Dehnen potential with a superposed softened Keplerian term corresponding to the central mass. From their work (their fig. 12), the relation between L and m can be compiled in a log–log scale. As shown in Fig. 4(a), one obtains a power-law fitting with $p \simeq 0.33$. Similarly, Merritt & Valluri (1996) computed the first and second (finite-time) LCNs of chaotic orbits in potentials corresponding to a galaxy with cuspy density profile and a central core radius. Their results can be compared to ours in the limit where the core radius (their parameter m_0) is larger than the sphere of influence of the central mass. This is the case $m_0 = 10^{-1}$ in table 1 of Merritt & Valluri (1996), compiled in log–log scale in Fig. 4(b). Apart from the value $m = 0$ (corresponding to the horizontal line going to $-\infty$), the three available data points appear also to be aligned in straight lines indicating power laws both for the first and the second Lyapunov exponent. The best-fitting exponents are $p \simeq 0.27$ and $\simeq 0.38$, respectively, while these values are only indicative due to the scarcity of data and the unknown influence of the central cusp of

the potential to the result. We note, finally, that the breaking of the power law and the appearance of a non-zero value of L as $m \rightarrow 0$ in Fig. 4(b) is due to a phenomenon called below ‘residual chaos’, i.e. chaos due to the cusp itself. This phenomenon is analysed in Section 4.

As an overall conclusion, a power law $L \sim m^p$ appears quite commonly in numerical computations of the Lyapunov exponents of the stellar orbits chaotically scattered by a central mass in various galactic models. We now proceed in a theoretical modelling allowing us to interpret the origin of this power law.

3 THEORETICAL MODELLING

3.1 Transit and out-of-transit dynamics

As mentioned in the Introduction, a modelling of the process of chaotic scattering of the orbits by the central mass becomes feasible by considering two distinct regimes of the motion, i.e. (i) transits

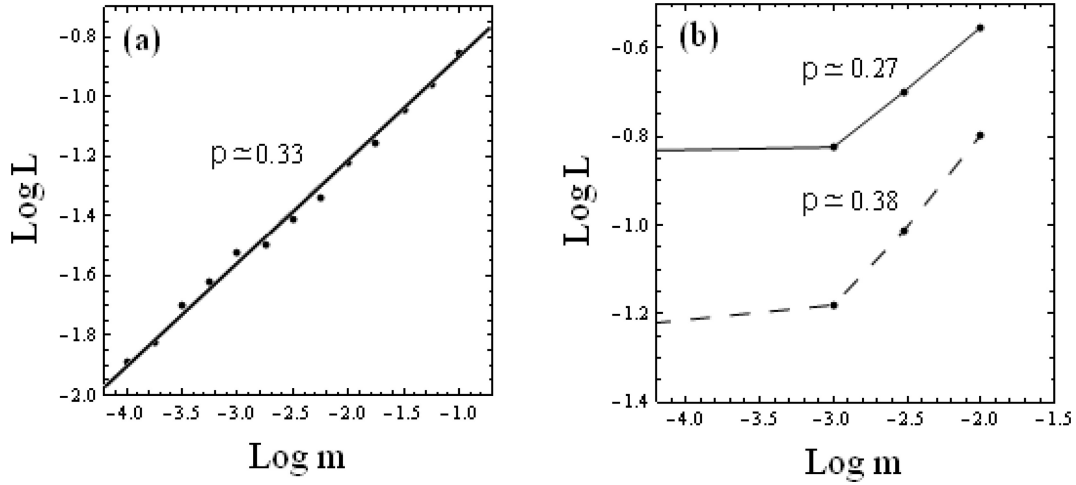


Figure 4. The L versus m relation as derived from the data of (a) Kandrup and Sideris (2002, lowest order approximation of a triaxial Dehnen potential), and (b) Merritt and Valluri (1996, potential corresponding to a galaxy with cusp). In (a), the compiled data confirm a power-law relation $L \sim m^p$ over the whole range of values of m considered. The solid line corresponds to a best fit yielding an exponent $p \approx 0.33$. In the right-hand panel (b) the solid and dashed lines show the dependence on m of the logarithms of the mean first and second Lyapunov exponents, respectively. Both lines extend to a non-zero value of $\log L$ for $m \rightarrow 0$. This represents the values corresponding to what is called ‘residual chaos’ in Section 4 below, i.e. chaos induced by the central cusp itself. The best-fitting exponents were computed in this case only by the three rightmost data points.

through the sphere of influence and (ii) out-of-transit oscillations. We begin by showing that within the out-of-transit regime the orbits obey three quasi-integrals of motion. Such integrals can be written as formal series, using, for example, the ‘third integral’ approach (Contopoulos 1960). A formal series has the form $\Phi = \Phi_2 + \Phi_3 + \dots$, where Φ_r are polynomial terms of degree r in the canonical variables (x, y, z, p_x, p_y, p_z) . The term Φ_2 is set equal to the harmonic energy in one of the three possible degrees of freedom, i.e. $(p_x^2 + \omega_x^2 x^2)/2$, $(p_y^2 + \omega_y^2 y^2)/2$, or $(p_z^2 + \omega_z^2 z^2)/2$. Terms of higher degree are computed recursively, by solving, order by order, the equation

$$\frac{d\Phi}{dt} = [\Phi, H_2 + H_4] = 0, \quad (10)$$

where $[\cdot, \cdot]$ denotes the Poisson bracket operator, and H_2, H_4 are the quadratic and quartic terms of the Hamiltonian (3). This means that the formal integrals are possible to define for the Hamiltonian neglecting the influence of the central mass. Then, we test numerically how well they are preserved in the full model, in the out-of-transit regime. Equation (10) yields, at degree r , the homological equation

$$[H_2, \Phi_r] = [\Phi_{r-2}, H_4]. \quad (11)$$

We used a computer-algebraic program to solve, step by step, the homological equation, for all three formal integrals defined as above, up to the 10th degree in the variables (x, y, z, p_x, p_y, p_z) . As an example, for the formal integral $\Phi_x = (p_x^2 + \omega_x^2 x^2)/2 + \dots$ up to 4th degree we have

$$\begin{aligned} \Phi_x = & 0.5x^2 + 0.5p_x^2 - \varepsilon (0.0025p_x^2p_y^2 - 0.007p_xp_y^3 \\ & - 0.0034p_x^2p_y p_z - 0.01p_xp_y^2p_z - 0.00125p_x^2p_z^2 \\ & + 0.0025p_y^2x^2 + 0.0034p_y p_zx^2 + 0.00125p_z^2x^2 \\ & - 0.01p_xp_yxy - 0.007p_y^2xy - 0.0052p_xp_zxy - 0.02p_y p_zxy \\ & - 0.0176p_xp_yy^2 + 0.01p_xp_zy^2 - 0.0152xy^3 \\ & - 0.0086p_xp_yxz + 0.01p_y^2xz - 0.005p_xp_zxz - 0.0017p_z^2yz \end{aligned}$$

$$\begin{aligned} & - 0.04p_xp_yyz + 0.0017x^2yz - 0.03xy^2z - 0.00125p_x^2z^2 \\ & - 0.00125x^2z^2) + O(\varepsilon^2). \end{aligned} \quad (12)$$

Similar expressions are found for the formal integrals Φ_y, Φ_z . The degree of approximation of these expressions can be tested by probing how well the integral values are preserved along individual orbits integrated first in the Hamiltonian $H = H_2 + H_4$ (i.e. without the central mass). For orbits in the energy range considered, we find that, up to $r = 10$, all three integrals are preserved to within a time variation of about $10^{-(4+r/2-2)}$ at the truncation order r . Fig. 5 shows an example of this behaviour. Panel (a) shows a comparison of the variations of the quantity Φ_x , computed as above, at the truncation orders $r = 4$ and 10 , for an example of box orbit with initial conditions as indicated in the panel. The maximum variation is about $\pm 2 \times 10^{-4}$ at the truncation order $r = 4$, but it reduces to about $\pm 3 \times 10^{-6}$ at the truncation order $r = 10$ (magnified in panel b). In fact, the estimates of Nekhoroshev theory (see e.g. Efthymiopoulos, Contopoulos & Giorgilli 2004) yield that the variations continue to decrease up to an optimal truncation order $r_{\text{opt}} \sim 1/(\varepsilon E)$, in which they become exponentially small, i.e. of order $O(\exp(-1/(\varepsilon E)))$. However, even low-order truncations are sufficient for estimating the values of the integrals Φ_x, Φ_y , and Φ_z in practice.

Restoring, now, the term $-m/(r^2 + d^2)^{1/2}$ in the potential, we compute the variation of all three quantities Φ_x, Φ_y, Φ_z during both transits and the out-of-transit regime. Fig. 6(a) shows the example of an orbit with initial conditions as in Fig. 5 (energy $E = 0.18$) in the case $m = 10^{-4}$, $\varepsilon = 0.1$. All three integrals are seen to exhibit abrupt jumps that coincide in time (e.g. at the times $t = 30, 52$, or 61 in Fig. 6a). A closer focus to the jump at $t = 52$ is shown in (Fig. 6b), superposing the variations of Φ_x in time with the variations of the distance of the orbit from the centre. Clearly, the most important jumps take place during transits through the sphere of influence of the central mass (which is about $2 \times 10^{-4/3} \approx 0.1$ in this case; see below, end of Section 3.1). A similar behaviour is found for the quasi-integrals Φ_y, Φ_z . On the other hand, the values of all three integrals are preserved to within two significant figures in the out-of-transit regime (without the central mass, the precision

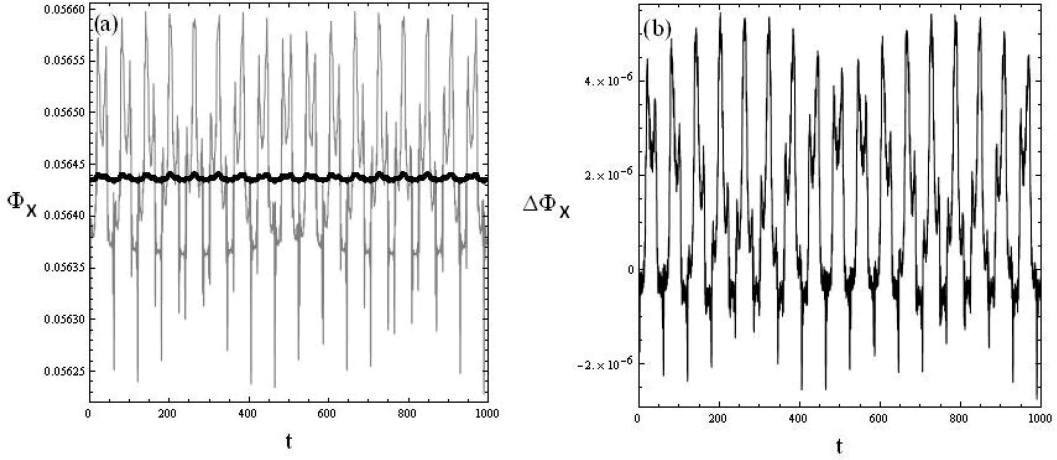


Figure 5. (a) Variations of the value of the formal integral Φ_x truncated at order 4 (thin line) or 10 (thick line) for an example of box orbit with initial conditions $x = 0.34$, $y = 0.23$, $z = 0.21$, $v_x = v_y = v_z = 0$. (b) The variations of the order 10 truncated series in greater detail (notice the change of scale in the vertical axis).

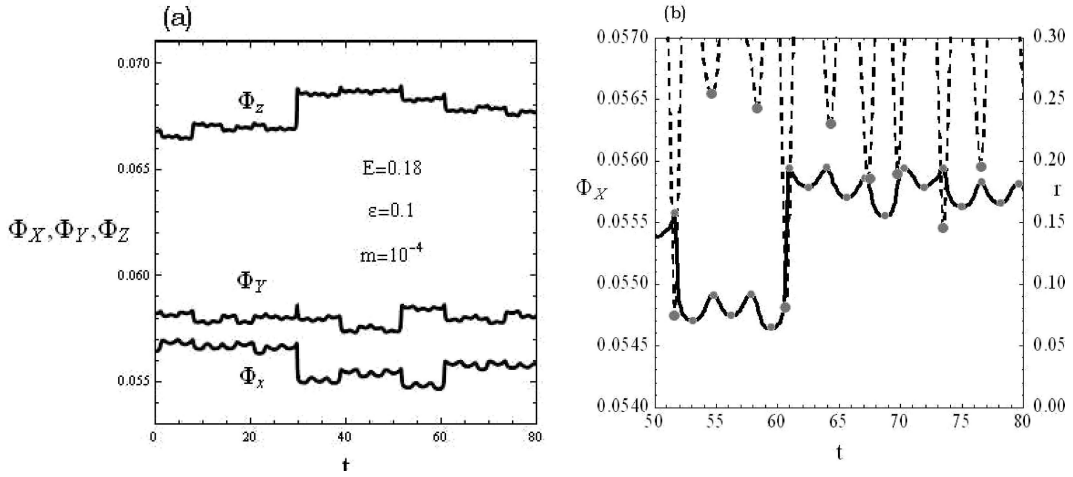


Figure 6. (a) Time evolution of the quantities Φ_x , Φ_y , Φ_z for one orbit with energy $E = 0.18$ in the experiment with $m = 10^{-4}$, $\varepsilon = 0.1$ (initial conditions as in Fig. 5). (b) The time evolution of Φ_x in detail (solid curve, corresponding to the scale of the left vertical axis), along with the time evolution of the orbit's distance from the centre (dashed curve, corresponding to the scale of the right vertical axis). Grey points on the latter curve correspond to local minima, while grey points on the Φ_x curve correspond to local extrema. Note that a local maximum of the curve $\Phi_x(t)$ coincides always with a local minimum of the curve $r(t)$.

increases to about four significant figures at the truncation order $r = 4$; see above). Fig. 7, now, compares the variations of $\Phi_x(t)$ for an orbit with the same initial conditions but different values of m and ε . The overall size of the variations appears rather insensitive on ε , while the size of all jumps (i.e. the difference between the value of Φ_x at the local maximum and minimum along a jump) clearly increases as m increases. One can observe also that the ‘landing’ value of $\Phi_x(t)$ at the end of one jump appears to be more and more unpredictable as m increases. Essentially, this uncertainty in the value of $\Phi_x(t)$ after each jump is a measure of the chaoticity of the orbit.

Quantifying the behaviour of the jumps after many transits allows us to see that the scattering of the orbits can be modelled essentially by Keplerian hyperbolic dynamics. Fig. 8(a) shows the mean value of the jumps $d\Phi_x$ (measured as the difference between the local maximum and minimum values of Φ_x at each jump) plotted against the mean value of the radii r_{\min} , where r_{\min} (computed from the data of Fig. 6b) means the radial distance from the central mass at the

point of closest approach during one jump. Both means are taken over the ensemble of all jumps during an integration of an orbit up to a time $t = 10^5$. The computation is repeated for different central mass values m , keeping the orbit's initial conditions fixed (same as in Fig. 6). During this time, the orbit exhibits some thousands of transits, thus the evaluation of mean values for both $d\Phi$ and r_{\min} has small statistical error. Fig. 8(a) shows the mean value of $d\Phi_x$ as a function of the mean value of r_{\min} , superposing the plots in log-log scale for the masses $m = 3 \times 10^{-5}$, 10^{-4} , 3×10^{-4} , 10^{-3} , and 3×10^{-3} . The straight fitting lines have inclination -1 , whereas we note that the vertical distance between two successive lines is about equal to $\log_{10} 3 \approx 0.5$. Thus, the mean jump $d\Phi_x$ is consistent with a (absolute) Keplerian potential law:

$$\overline{d\Phi_x} \approx \frac{m}{r_{\min}}. \quad (13)$$

The above result concerns the variations of the quasi-integrals valid in the out-of-transit regime. On the other hand, inside the sphere

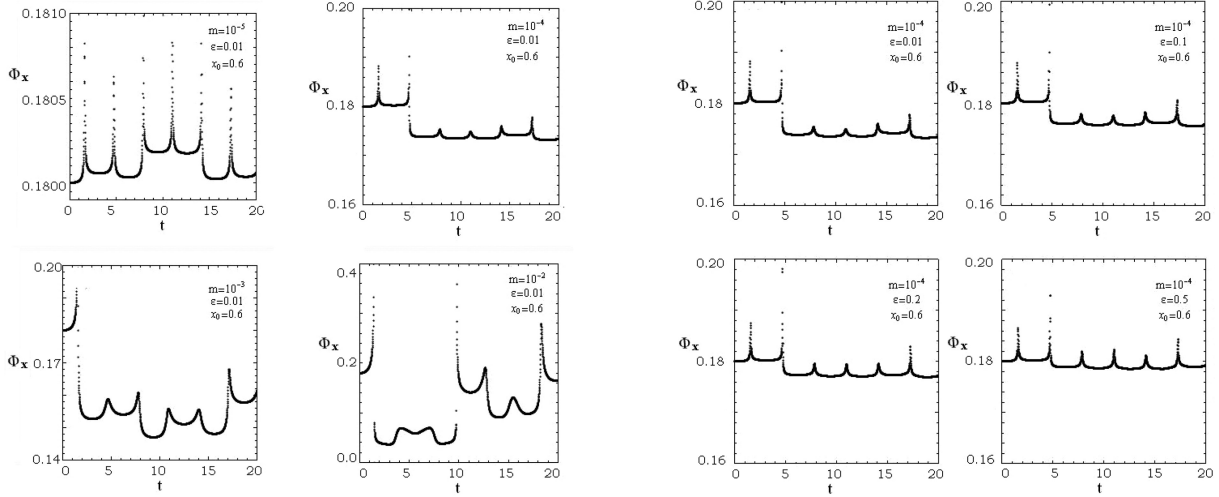


Figure 7. Variations of $\Phi_x(t)$ for an orbit with energy $E = 0.18$ and four different values of m (left), or ϵ (right). The values of (μ, ϵ) are indicated in the figure. Note the change of scale in the ordinate of the four left-hand panels, indicating that the variations of the quasi-integral depend strongly on the value of the mass parameter (while they are nearly insensitive to the non-linearity parameter ϵ as long as the latter is not very close to unity).

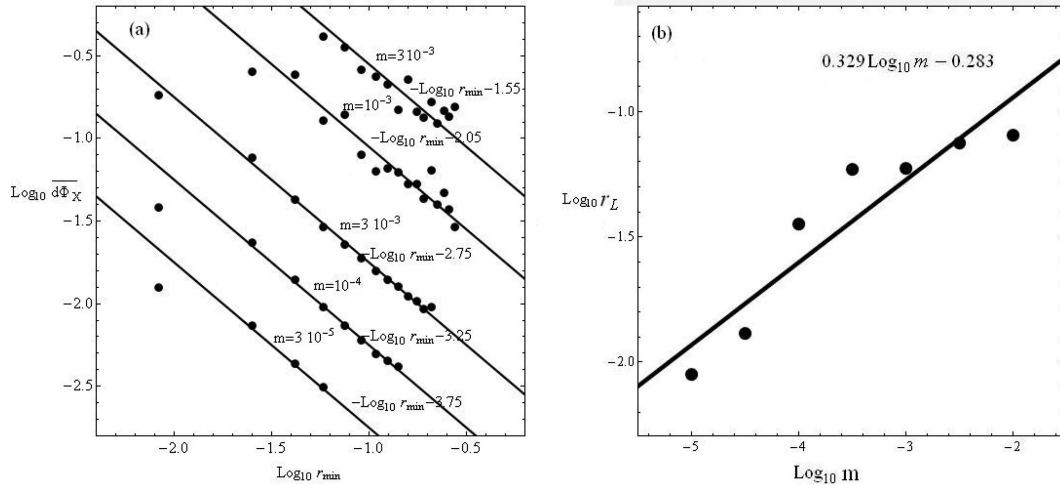


Figure 8. (a) The points represent the logarithm of the mean absolute value of the Φ_x integral's jumps $\log d\Phi_x$ for different values of the central mass parameter, versus the logarithm of the mean minimum distance r_{\min} from the central mass over all transits for chaotic orbits with initial conditions as in Fig. 6. The fitting straight lines have equation as indicated in the figure. (b) The mean radius r_L within which the angular momentum is approximately conserved (see text) versus m .

of influence the force field is approximately central, thus another approximate integral, of the angular momentum L , is valid. During transits, we follow the time variations of L and determine, at each transit separately, the maximum radius r_L up to which the variations ΔL are smaller in size than a fixed percentage of L (taken as 10 percent difference measured from the value of L at the point of closest approach to the central mass). Fig. 8(b) shows the so-obtained mean value of r_L as function of the central mass parameter m in log–log scale for the same orbits as in Fig. 8(a). Albeit with considerable scatter, the data allow us to determine a best-fitting power law $r_L \approx 2.2m^{0.329}$. This is close to the power law for the sphere of influence (equation 5), thus allowing us to identify r_L as a measure of r_m yielding the estimate $r_c \approx 2$. We note that the threshold of 10 per cent variation of the angular momentum is rather arbitrary. However, it allows us to obtain a meaningful result for box orbits which, far from the BH sphere of influence, undergo angular momentum

variations of order 100 per cent (with more stringent thresholds, we identify significantly fewer transitions through the BH sphere of influence). In conclusion, their scatter notwithstanding, the previous plots suggest a qualitative picture in which the dynamics of chaotically scattered centrophilic orbits can be modelled as a sequence of (i) transits through the sphere of influence, in which the orbits follow approximately a Keplerian hyperbolic dynamics, followed by (ii) box-like wanderings within the rest of the available space in the interior of the equipotential ellipsoid corresponding to a fixed value of the orbital energy. This picture is quite generic when the three frequencies $\omega_1, \omega_2, \omega_3$ are far from low-order commensurabilities. The generation of such commensurabilities necessitates a separate treatment, since, then, the orbital sample contains also many resonant boxlets (Miralda-Escudé & Schwarzschild 1989). In our model, boxlets corresponding to low-order commensurabilities are generated by the quartic potential terms in equation (4) for large

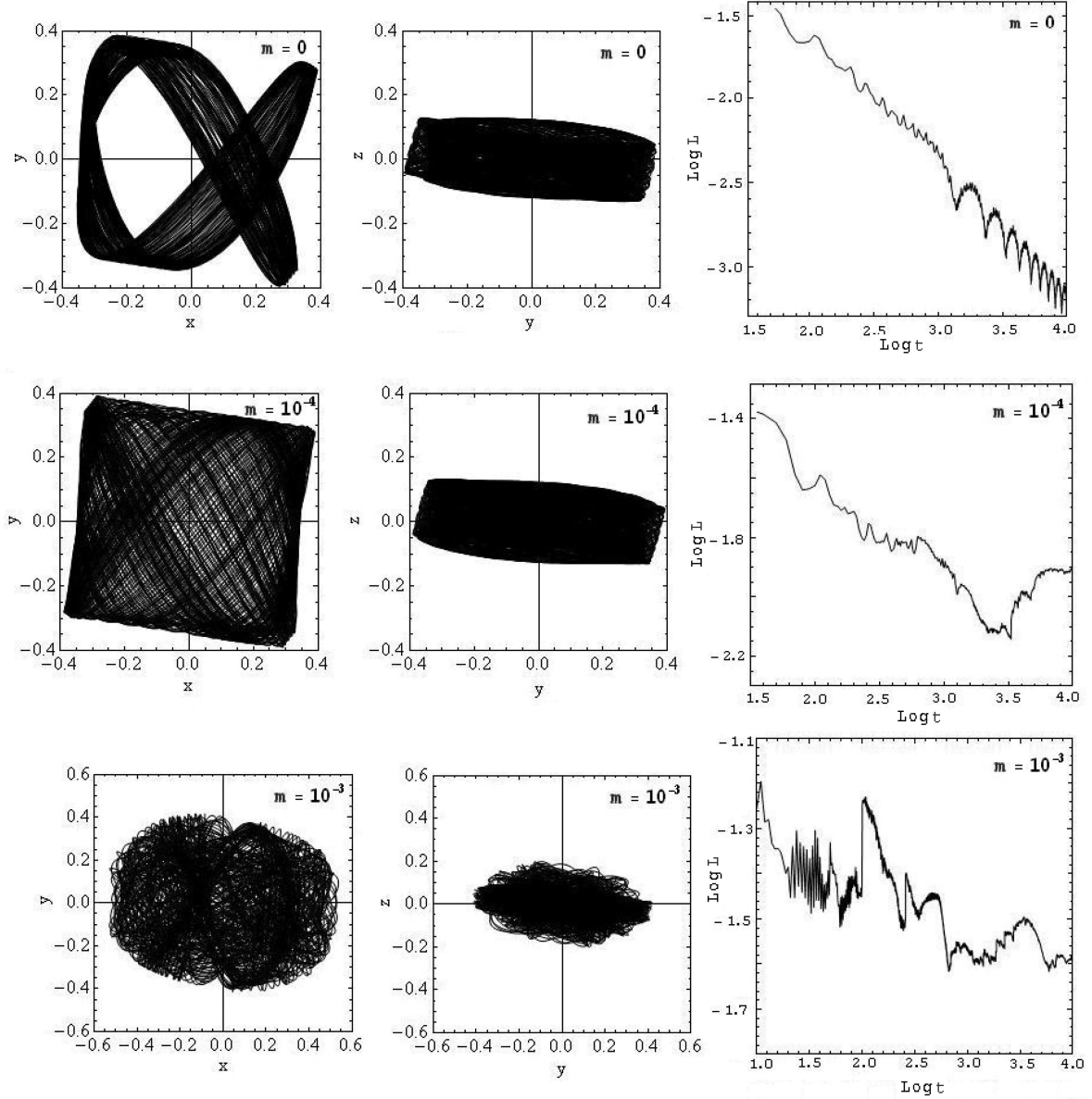


Figure 9. Upper row: projection of a thin tube orbit around a ‘boxlet’ 3:2 periodic orbit in the planes (x, y) (left-hand panel), and (y, z) (middle panel), along with the evolution of its finite-time Lyapunov exponent $\chi(t)$ (right-hand panel). The central mass parameter is set equal to $m = 0$, and the non-linearity parameter $\varepsilon = 0.9$. The orbit’s initial conditions are: $x = 0.1894$, $y = -0.04796$, $z = 0.0014$, $v_x = -0.3578$, $v_y = -0.4682$, $v_z = -0.097$. The orbital energy is $E = 0.193$. Middle and lower rows: same as in the upper row, but with a central mass $m = 10^{-4}$ and 10^{-3} , respectively.

($\mathcal{O}(1)$) values of ε . An example is given in Fig. 9, for $\varepsilon = 0.9$. When $m = 0$ (top row) the orbit with initial conditions as indicated in the figure’s caption is a three-dimensional thin-tube orbit around a resonant 3: 2 orbit which exists in the plane (x, y) . The periodic orbit is stable, and, hence, centrophobic (Merritt & Valluri 1999). In Fig. 9, top row, the tube orbit around the boxlet also avoids the centre. Hence, it is a regular orbit, as confirmed by computing its Lyapunov characteristic exponent (right-hand panel), which goes to zero. Now, the orbit’s closest approach to the centre is at a distance $r \sim 2 \times 10^{-2}$. Thus, by adding a central mass with parameter $m = 10^{-4}$ (middle row), the orbit now crosses the central mass sphere of influence (of radius $\sim 10^{-4/3}$). As a result, we observe that the orbit is significantly deformed, and loses its resonant character, while the Lyapunov exponent stabilizes to a positive value $\sim 10^{-2}$, i.e. the

orbit becomes weakly chaotic. For still larger m ($m = 10^{-3}$), the orbit exhibits the usual behaviour of a chaotic centrophilic orbit, with a Lyapunov exponent $\sim 2.5 \times 10^{-2}$.

We now model the chaotic scattering process of centrophilic orbits in order to derive theoretical estimates for the orbits’ Lyapunov exponents.

3.2 Theoretical Estimates on Lyapunov Exponents

Consider an orbit integrated along with the variational vector $\xi(t)$ of a nearby orbit up to the time t . Let ξ_i be the modulus of the deviation vector of the orbit at the time $t_i = i\Delta t$, where $\Delta t = t/n$ is the time step corresponding to a splitting of the integration in n

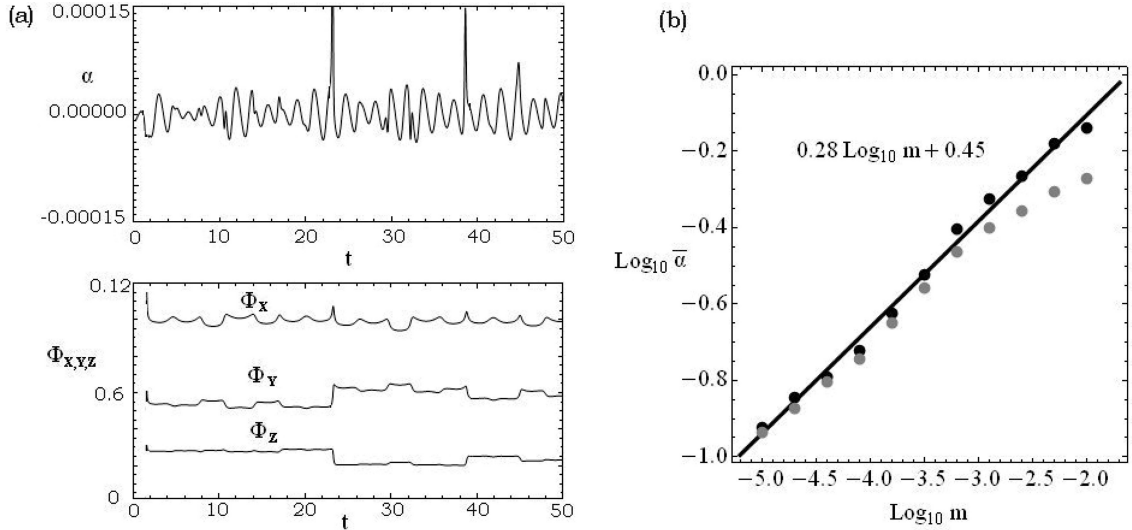


Figure 10. (a) Comparison of the time evolution of the stretching number $a(t)$ (equation 14) with the variations of the quasi-integrals Φ_x , Φ_y , Φ_z . (b) The mean stretching number \bar{a} after thousands of transits versus m for the orbit with same initial conditions as in Fig. 6. A power-law fit yields $\bar{a} \propto m^{0.28}$. The theoretical estimate $\bar{a} \propto m^{1/3}$ is found in the Appendix.

steps. The *stretching number* Voglis & Contopoulos (1994) at the i th step is defined as

$$a_i = \frac{1}{\Delta t} \ln \frac{\xi_i}{\xi_{i-1}}. \quad (14)$$

The finite-time LCN is equal to the mean stretching number along the orbit, since

$$\chi(t) = \frac{1}{t} \ln \frac{\xi(t)}{\xi_0} = \frac{1}{n\Delta t} \sum_{i=1}^n \ln \frac{\xi_i}{\xi_{i-1}} = \frac{1}{n} \sum_{i=1}^n a_i. \quad (15)$$

Fig. 10(a) shows the time evolution of the stretching number $a(t)$ as a function of time, along with the variations of the integral $\Phi_x(t)$ for the orbit with initial conditions as in Fig. 7, for $m = 10^{-3}$, $\varepsilon = 0.1$. Far from transits, the function $a(t)$ shows an oscillatory behaviour around zero. This behaviour is characteristic of a nearly-harmonic oscillation, while the quartic potential term implies an overall linear growth of the deviation vector in the out-of-transit regime, which is of order $O(\varepsilon)t$. On the other hand, in Fig. 10(a) the curve $a(t)$ clearly exhibits positive peaks at all transits.

Consider the set $\mathcal{S} = \{i_1, i_2, \dots, i_{n_T}\}$ such that the orbit is in transit at the time t_i with $i \in \mathcal{S}$, n_T denoting the total number of time steps during which the orbit is in the transit phase. Let $\bar{\mathcal{S}}$ be the complement of \mathcal{S} with respect to the set $\{1, 2, \dots, n\}$. One has the estimate

$$\frac{1}{n\Delta t} \sum_{i_j \in \bar{\mathcal{S}}, j=1}^{n-n_T} \ln \frac{\xi_{i_j}}{\xi_{i_j-1}} \approx O\left(\frac{\ln(\varepsilon n\Delta t)}{n\Delta t}\right),$$

implying that the contribution of the ‘out-of-transit’ stretching numbers to the final value of $\chi(t)$ goes to zero as $\sim \ln t/t$. Thus, one has the approximation

$$\chi(t) \approx \frac{1}{n\Delta t} \sum_{i_j \in \mathcal{S}, j=1}^{n_T} a_{i_j}.$$

Setting $\bar{a} = (1/n_T) \sum_{i_j \in \mathcal{S}, j=1}^{n_T} a_{i_j}$ we get $\chi(t) \approx (n_T/n\Delta t)\bar{a}$. The quantity

$$N_{\text{vis}} = \frac{n_T}{n\Delta t},$$

hereafter called ‘rate or visits’, represents the number of transits per unit period of an orbit within the sphere of influence. We then have

$$\chi(t) \approx N_{\text{vis}} \bar{a}. \quad (16)$$

Estimates on the mean value of $\chi(t)$ for all transiting orbits at fixed central mass parameter m will then follow by estimating separately the quantities \bar{a} and N_{vis} .

Assuming, as evidenced above, that the transits are governed by nearly-Keplerian hyperbolic dynamics, in the appendix it is shown that for orbits of given energy E , one has the theoretical estimate

$$\bar{a} \propto \frac{m^{1/3}}{E^{1/2}}. \quad (17)$$

Fig. 10(b) shows the mean a computed numerically for an orbit of fixed energy with the same initial conditions as in Fig. 6, integrated under various values of m . Numerically we find the exponent 0.28, which is in fair agreement with the theoretical exponent $1/3$ of equation (17). The predicted dependence of \bar{a} on the energy, probed numerically below, is also verified. We now focus on estimating N_{vis} . The frequency whereby an orbit visits the sphere r_m depends on the geometry of the orbit in configuration space. We distinguish two cases, explained with the help of Fig. 11.

(i) *3D orbit*: as long as the three quantities Φ_x , Φ_y , Φ_z obtain comparable values, an orbit fills nearly uniformly the available configuration space, which has the form of a deformed 3D box.

(ii) *Planar orbit*: at least one of the three quantities Φ_x , Φ_y , Φ_z obtains a value smaller than a given threshold (given by equation 18 below). Geometrically, the amplitude of oscillations in at least one of the three axes in the out-of-transit regime should be smaller than the radius r_m of the sphere of influence (Fig. 11a, schematic). Quantitatively

$$(2\Phi_k/\omega_k^2)^{1/2} < r_m, \quad (18)$$

where k stands for x , y , or z .

Note that ‘linear’ orbits, i.e. tubes around the stable axial orbits also exist, but their importance is rather limited because they are considerably fewer than the planar or 3D orbits.

The dependence of the rate of visits to the central masses’ sphere of influence on the geometry of orbits can be modelled in the

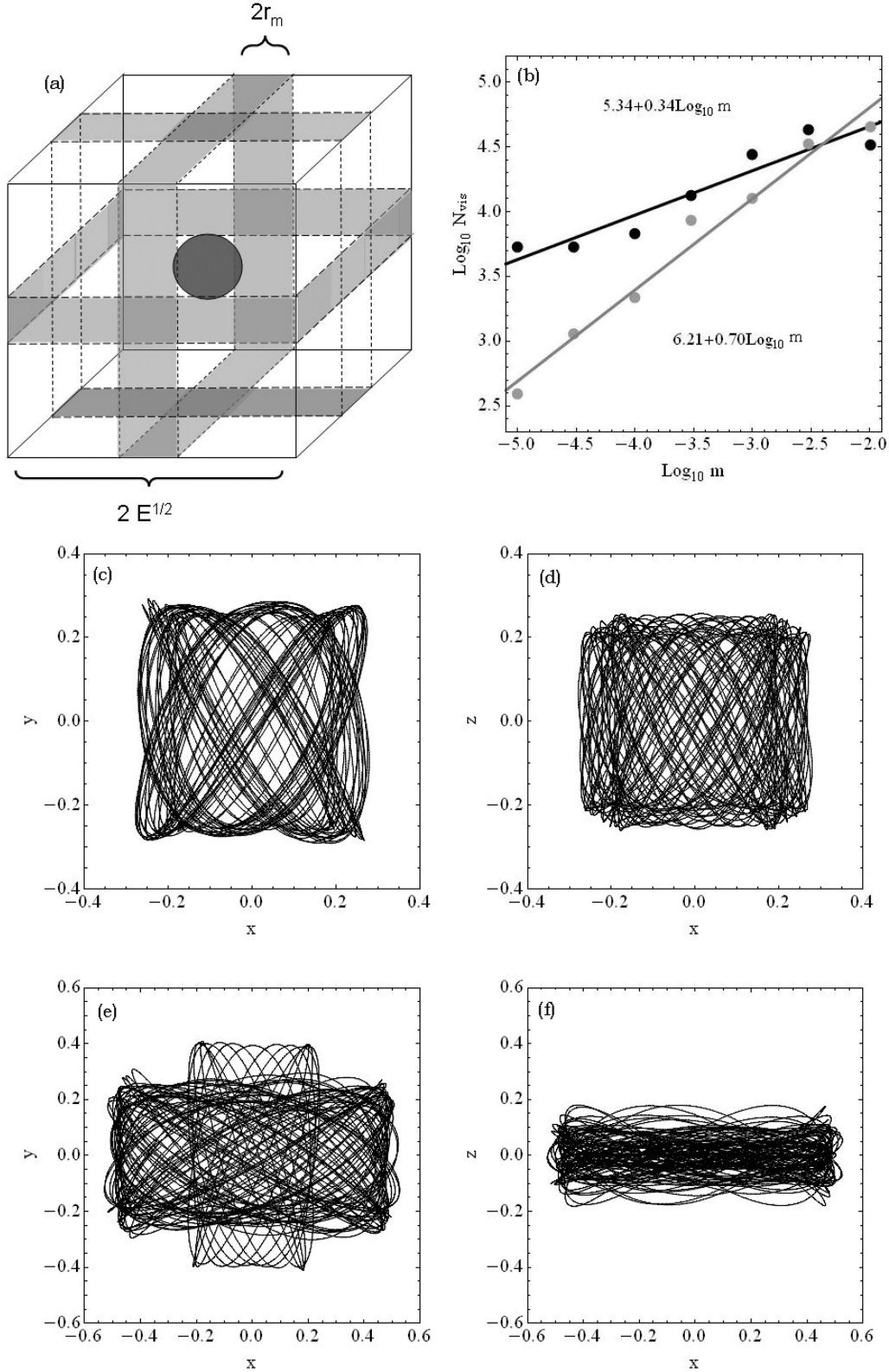


Figure 11. (a) Schematic representation of the configuration space of motion of ‘3D orbits’ and ‘planar’ orbits. The cube represents a box volume covered by a ‘3D orbit’. The central sphere represents the central mass sphere of influence. The three thin parallelepipeds (grey) correspond to one parallelepiped side being equal to $2r_m$. Planar orbits are orbits lying inside one of the three parallelepipeds. (b) The number of visits (up to time $t = 10^5$) versus m for two orbits characterized as ‘3D’ (black points, initial conditions $x = 0.227$, $y = 0.155$, $z = 0.139$, $v_x = v_y = v_z = 0$), and ‘planar’ (grey points, initial conditions $x = 0.227$, $y = 0.155$, $z = 0.0$, $v_x = v_y = v_z = 0$), for $\varepsilon = 0.1$. The straight lines represent power-law fittings yielding the best-fitting exponents 0.7 and 0.34, respectively. (c)–(d) Projection of the ‘3D’ orbit in the planes (x, y) and (x, z) . (e)–(f) Same for the ‘planar’ orbit. Note in (e) the change in morphology induced by a big jump in the values of the quasi-integrals Φ_x , Φ_y . Such jumps are stochastic in nature, and they may occasionally convert a 3D orbit to planar and vice versa.

following way: for 3D orbits, considering all possible straight line segments connecting two different points on the surface of the box delimiting the orbit (see Fig. 11a), N_{vis} can be approximated as proportional to the percentage or line segments passing through the sphere of influence. Then, $N_{\text{vis}} \propto S_{r_m}/S_{\text{tot}}$, where S_{r_m} and S_{tot} are the surface of the sphere of influence and of the box, respectively. The linear dimension of the box is of order $l \sim E^{1/2}$, where E is the energy of the orbit. Thus, $N_{\text{vis}} \propto r_m^2/E$, or (taking into account equation 5)

$$N_{\text{vis}} \propto \frac{m^{2/3}}{E}. \quad (19)$$

For planar orbits, one has, instead, the estimate $N'_{\text{vis}} \propto r_m/l$, or

$$N'_{\text{vis}} \propto \frac{r_m}{E^{1/2}} = \frac{m^{1/3}}{E^{1/2}}. \quad (20)$$

These estimates are confirmed numerically. Fig. 11(b) shows a computation of the rate of visits N_{vis} , N'_{vis} for two orbits with constant energy $E = 0.18$, but for different mass parameters m . The number of visits within a total integration time $t = 10^5$ are counted, and cri-

terion (18) is used in order to distinguish either orbit as ‘planar’ or 3D (the corresponding rate of visits is found by dividing the number of visits by $t = 10^5$). The difference in the shape of the orbits is evident (Figs 11c–f). Returning to Fig. 11(b), the best-fitting exponents of the relations N_{vis} and N'_{vis} to m are 0.7 and 0.34, respectively, in fair agreement with equations (19) and (20) for constant E . Taking into account equations (20), (19), and (17) we find for the Lyapunov number of 3D orbits of energy E the estimate

$$\chi \approx \frac{m^{2/3}}{E} \times \frac{m^{1/3}}{E^{1/2}} \approx \frac{m}{E^{3/2}}, \quad (21)$$

whereas, for planar orbits

$$\chi' \approx \frac{m^{1/3}}{E^{1/2}} \times \frac{m^{1/3}}{E^{1/2}} \approx \frac{m^{2/3}}{E}. \quad (22)$$

Fig. 12(a) shows the values of $\log \chi$ against $\log E$ for all the orbits in our considered ensembles for six different values of the mass parameter m as indicated in the caption. The various ensembles are clearly distinguished by the concentration of points in the scatter plot, the uppermost concentration corresponding to the ensemble in

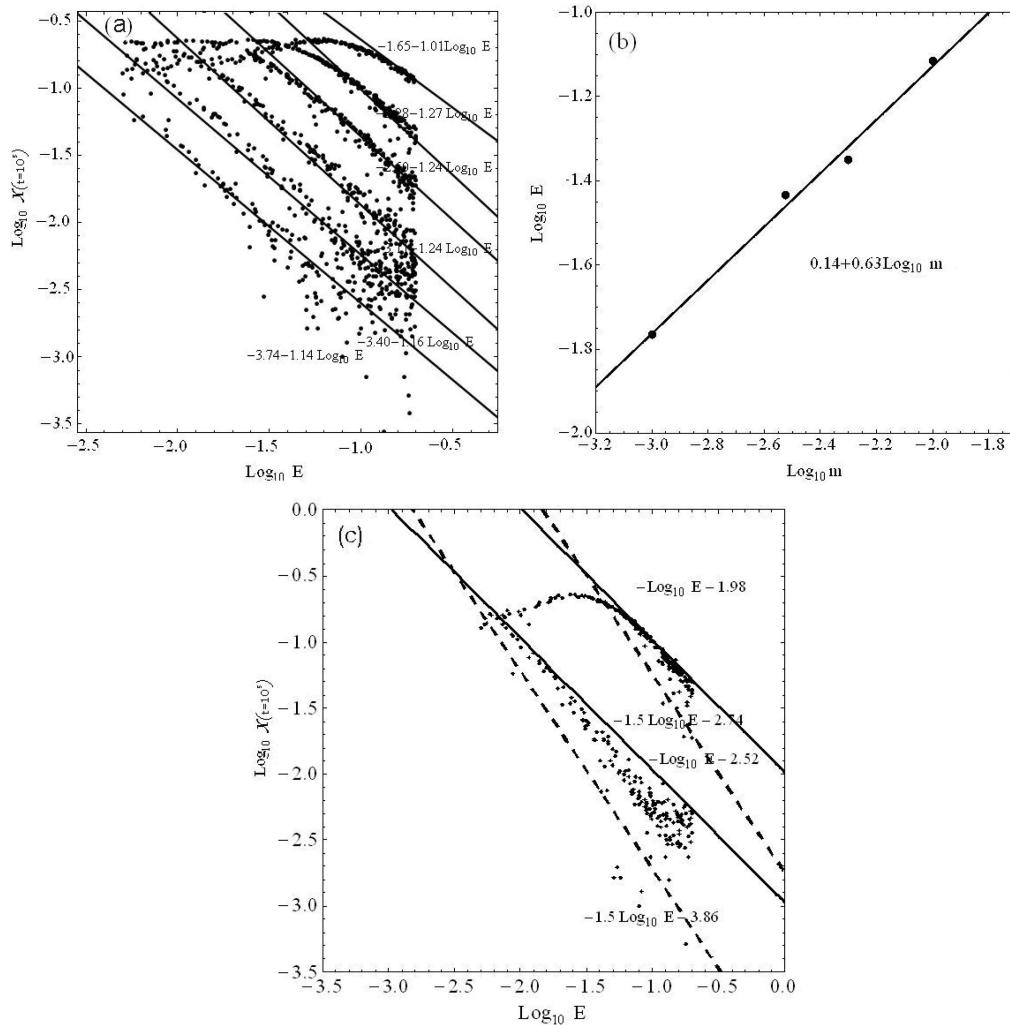


Figure 12. (a) The logarithms of finite-time LCNs $\log \chi$ of all orbits in the chosen ensembles versus the logarithm of the orbital energy $\log E$ for the experiments with mass parameters (from top to bottom) $m = 10^{-2}$, 3×10^{-3} , 10^{-3} , 3×10^{-4} , 10^{-4} , and 3×10^{-5} , at the end of the integration ($t = 10^5$). The straight lines represent asymptotic power-law fittings for the right parts of the plots separately for each mass parameter. (b) The energy E_{max} where $\log \chi$ in (a) exhibits a global maximum versus m . The power-law fitting is $E_{\text{max}} = 2.2m^{2/3}$. (c) The plot $\log \chi$ versus $\log E$ in greater detail for the masses $m = 3 \times 10^{-3}$ and 3×10^{-4} . In each case, numerical values are distributed between two lines with inclination -1 and -1.5 , as predicted from equations (22) and (21) for the planar and the 3D orbits, respectively.

the experiment with the highest mass parameter ($m = 10^{-2}$). Each ensemble can be roughly described as consisting of a ‘rising’ and a ‘falling’ part of the value of $\log \chi$ versus $\log E$. The two parts meet at a point of maximum of $\log \chi$. The position of the maximum moves to the right with respect to $\log E$ as m increases. However, the level value of $\log \chi$ at the maximum remains remarkably constant, i.e. nearly independent of m .

The straight lines show power-law fittings of χ with E for the falling part. Despite the large scatter of the data points, we find indicative logarithmic slopes lying in the range between -1 and -1.5 for all ensembles considered. This behaviour will be explained below. A power law roughly holds also in the rising part. The point of maximum corresponds to about the point where the associated best-fitting power laws intersect. The intersection point defines an energy E_c . Computing and plotting E_c against m yields approximately a power law $E_c \propto m^{0.63}$ (Fig. 12b).

These features can be understood by the following considerations: first, one can note that the left part represents regular or sticky chaotic orbits which have the morphology of *pyramids* (Merritt & Vasiliev 2011), i.e. they lie nearly entirely within the sphere of influence of the central mass. Such orbits can be described by perturbations to the Keplerian dynamics of the central mass. The limiting energy value E_l up to which an orbit lies entirely within the radius $r = r_m$ can be estimated by requiring that the sphere $r = r_m$ constitutes the surface of zero-velocity. The estimate

$$E_l \approx \frac{1}{2} \Omega^2 r_m^2 - \frac{m}{r_m} \approx \frac{1}{2} \Omega^2 r_c^2 m^{2/3} - \frac{m}{r_c} = \left(\frac{r_c^2 \Omega^2}{2} - \frac{1}{r_c} \right) m^{2/3} \quad (23)$$

holds, where Ω is a geometric-mean estimate of the harmonic frequencies, bounded by the highest of the three frequencies ω_x , ω_y , ω_z . The dependence of E_l on m in equation (23) has the exponent 0.66, close to the exponent in the numerical fitting of E_c versus m (Fig. 12b). This suggests that $E_l \simeq E_c$ (the near equality holds also checking numerical versus theoretical coefficients). Use of the estimate (23) is made in the next subsection.

On the other hand, most chaotic orbits lie beyond the energy E_{\max} . In fact, isolating the plots $\log \chi$ versus $\log E$ (Fig. 12c) for two values of the mass parameter m allows us to see that the whole ensemble of orbits in the right wing are delimited between two limiting lines with inclinations -1 and -1.5 , respectively, i.e. as predicted from the estimates of equations (22) and (21) for the planar and the 3D orbits, respectively. The coexistence of ‘planar’ and ‘3D’ orbits explains in this way the scatter in the data points of Fig. 12(a).

3.3 Final theoretical estimates: the power law $L \propto m^p$

Assuming (as evidenced in Fig. 1b) that a time $t = 10^5$ is sufficient for a saturation of $\chi(t)$ close to the limiting value of chaotic orbits, i.e. close to the LCN, the mean LCN of the orbits in an energy range $E_{\min} \leq E \leq E_{\max}$ can be estimated as

$$L \approx \frac{1}{N_0} \int_{E_{\min}}^{E_{\max}} N(E) \bar{\chi}(t = 10^5, E) dE, \quad (24)$$

where $N_0 = \int_{E_{\min}}^{E_{\max}} N(E) dE$, $N(E)$ is the number density of orbits of energy E , and $\bar{\chi}(t = 10^5, E)$ is a mean estimate of the value of χ for orbits of energy E at the final integration time. Considering only transiting orbits, we set $E_{\min} = E_l \sim m^{2/3}$ (equation 23). Also, from Fig. 12(a) it is clear that the maximum energy $E_{\max} = 0.2$ considered in our samples is sufficiently high for the orbits’ values

of χ to fall with respect to the maximum by at least one order of magnitude in the worst case ($m = 10^{-2}$), and typically by several orders of magnitude.

The mean value $\bar{\chi}(t = 10^5, E)$ can be now estimated by considering the separate mean values of χ as well as an E -dependent varying proportion of planar versus 3D orbits. The percentage λ of the planar orbits is estimated by the ratio of the surface occupied by initial conditions of planar orbits on the box surface corresponding to an energy level E (see Fig. 11a) over the total area of the box. Thus

$$\lambda = \frac{S_{2d}}{S_{\text{tot}}} \approx \frac{48 E^{1/2} r_m}{24 E} \approx \frac{2 m^{1/3}}{E^{1/2}}. \quad (25)$$

The percentage of 3D orbits is $1 - \lambda \approx 1 - 2 m^{1/3} / E^{1/2}$. Finally, $\bar{\chi}$ is estimated according to equations (21), (22), i.e.

$$\bar{\chi}_{\text{planar}}(E) \approx c_1 \frac{m^{2/3}}{E}, \quad \bar{\chi}_{3D}(E) \approx c_2 \frac{m}{E^{3/2}}, \quad (26)$$

with c_1 and c_2 being constants of order unity. Then, for the mean value of χ at fixed energy we have the estimate

$$\bar{\chi}(E) \approx \lambda \bar{\chi}_{\text{planar}}(E) + (1 - \lambda) \bar{\chi}_{3D}(E). \quad (27)$$

The main uncertainty in equation (24) regards the form of the number density function $N(E)$. In self-consistent models, $N(E)$ is determined by the distribution function of the centrophilic orbits. On the contrary, in ‘ad hoc’ potential models, $N(E)$ cannot be determined self-consistently unless one possesses information on the kinematic distributions allowing us to solve the reverse problem $\text{density} \rightarrow N(E)$. Assuming no detailed model, we hereby estimate the integral of equation (24) using two different estimates of $N(E)$ as follows.

(i) We consider the case of a nearly uniform distribution $N(E) = \text{const}$. Combining equations (24), (27), and (26) we obtain:

$$L \approx \frac{1}{0.2 - m^{2/3}} [4c_1 m^{2/3} + 10c_2 m^{4/3} - 2.23(4c_1 + 2c_2)m]. \quad (28)$$

The exact dependence of L on m in the model (28) depends on the relative values of the constants c_1 and c_2 , as well as on factors entering in all the above estimates. Fig. 13(a) shows L against m in logarithmic scale, by the estimate (28) (black points) setting simply $c_1 = c_2 = 1$. The plot indicates an approximate power law $L \sim m^p$. This is produced as follows: since m is a small quantity, the leading term in equation (28) is the one with lowest exponent, i.e. $m^{2/3}$. Thus, in the absence of additional terms, we would have $p = 2/3$. However, for relatively large m , the second most important term (linear in m) has a negative sign. Thus, it lowers the rightmost part of the curve L versus m (the presence of $m^{2/3}$ in the denominator only marginally affects the overall power-law behaviour). If we approximate the new curve by a single power-law fitting, we then find a lowering of the exponent p , i.e.

$$L \propto m^{2/3-q}, \quad (29)$$

with q varying between 0.1 and 0.2. However, one notices that the whole curve in log-log scale deviates downwards from the power-law approximation (29) for the highest mass parameter values, i.e. q has a weak (increasing) dependence on increasing m . Comparison with the numerical data (grey dots, for $\varepsilon = 0.1$) shows that the model reproduces the slope of the numerical curve, which also exhibits a lowering of the value of L at high mass parameter values with respect to an exact power law. Overall, the theoretical curve has a factor ≈ 2 difference from the numerical curve, which is consistent

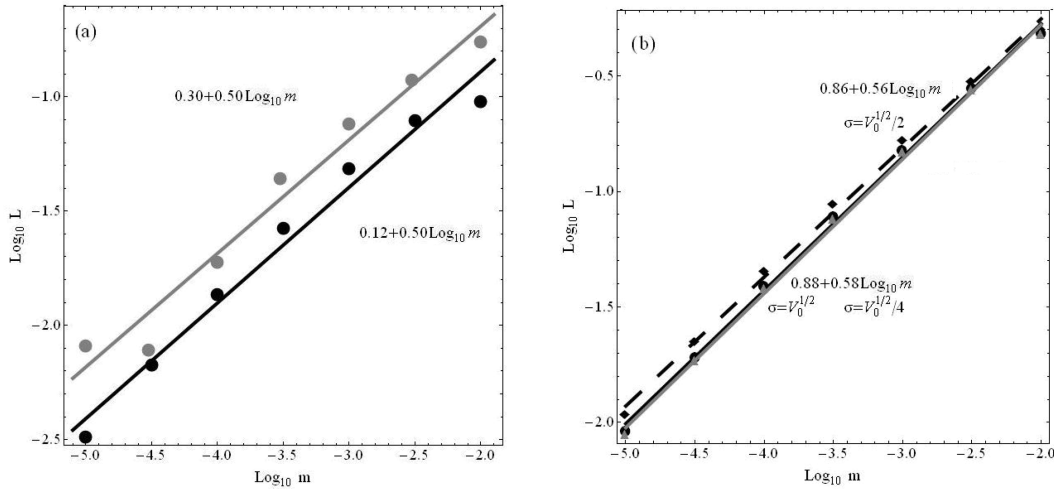


Figure 13. (a) Mean finite LCN L versus the mass parameter m as it follows theoretically from equation (28) (black dots), compared to the numerical computation (grey dots) at the integration time $t = 10^5$, for all the experiments with $\varepsilon = 0.1$. The mean inclination is close to 0.5 in the range $10^{-5} < m < 10^{-2}$. (b) Theoretical computation of L versus m in an ‘isothermal’ number density model (see text). The triangles and grey fitting line correspond to the choice $\sigma = V_0^{1/2}/4$, filled circles and black solid line to $\sigma = V_0^{1/2}/2$, squares and dashed line to $\sigma = V_0^{1/2}$.

with uncertainties in the theoretical coefficients. Note also that a systematic lowering of the values of L with respect to a power-law fitting is discernible in all the plots of Fig. 3. Finally, we have checked that the appearance of an approximate power law persists, with exponents around $p \approx 0.5$, for different choices of the constants c_1 and c_2 . This shows that the dependence of the integral (24) on m (which enters in the integral as a parameter) is not sensitive on the details of the distribution of the planar versus 3D orbits.

(ii) Fig. 13(b) shows an evaluation of the integral (24) for an isothermal (or ‘ergodic’; see Binney & Tremaine 2008) model of $N(E)$, i.e. $N(E) \propto e^{-E/\sigma^2}$. The constant σ is a measure of the velocity dispersion in the central parts of the galaxy. Assuming a core density $\rho \approx 3/(4\pi)$ (in our units, corresponding to total mass $M = 1$ at radius $R = 1$), by the Virial theorem σ^2 has to be taken to be of the order of the absolute value of the central potential well $V_0 \approx \int_0^1 4\pi G \rho r dr \approx 1.5$. Fig. 13(b) shows the evaluation of the integral (24) for three different choices of σ , namely $\sigma = V_0^{1/2}$, $\sigma = (1/2)V_0^{1/2}$, and $\sigma = (1/4)V_0^{1/2}$. In all three cases we recover here as well an effective power-law behaviour, with not very different exponents, i.e. $p \approx 0.58$, ≈ 0.56 , and ≈ 0.56 , respectively.

In conclusion, we find that an approximate power-law relation of the form (29) is robust against details of the form of the function $N(E)$.

4 EFFECT OF CENTRAL CUSP

In the model (4), the existence of many box orbits was a priori guaranteed due to the harmonic core in the centre. It is well known, however, that realistic models of the central parts of galaxies include central density cusps $\rho(r) \sim r^{-\gamma}$ (see e.g. the review in Binney & Merrifield 1998, or Merritt 1999). In such models, the cusp itself transforms most centrophilic orbits to chaotic (Merritt & Valluri 1996; Merritt & Quinlan 1998). Even without central BH, one then expects the orbits to exhibit positive Lyapunov exponents. We hereafter call this effect ‘residual chaos’, i.e. chaos existing even when $m = 0$. The corresponding mean Lyapunov exponent of the centrophilic orbits is denoted by L_0 .

Adding, now, a central mass ($m \neq 0$) we seek to determine the dependence of L on m . The theoretical analysis of the previous section formally breaks down, since one cannot define the formal integrals Φ_x , Φ_y , Φ_z , even for $m = 0$. We thus rely on numerical computations. To this end, we consider again the Hamiltonian function (3), changing the potential model to

$$V = V_D - \frac{m}{(r^2 + d^2)^{1/2}}, \quad (30)$$

where V_D represents the ellipsoidal Dehnen model (Dehnen 1993):

$$V_D(x, y, z) = -\pi Gabc \int_0^\infty \frac{[\psi(\infty) - \psi(w)]d\tau}{\sqrt{(\tau + a^2)(\tau + b^2)(\tau + c^2)}}, \quad (31)$$

where

$$\psi(w) = \int_0^w \rho(w'^2)dw'^2,$$

with

$$w^2 = \frac{x^2}{a^2} + \frac{y^2}{b^2} + \frac{z^2}{c^2}, \quad a \geq b \geq c > 0,$$

and $\rho(w)$ given by

$$\rho(w) = \frac{(3 - \gamma)M}{4\pi abc} w^{-\gamma} (1 + w)^{-4+\gamma}, \quad 0 \leq \gamma < 3. \quad (32)$$

The parameters a , b , and c correspond to the lengths of the major, intermediate, and minor axis of the triaxial equipotential surface corresponding to $w = 1$. The parameter M determines the system’s total mass. We use a similar algorithm as in Merritt & Fridman (1996) in order to numerically evaluate the integral (31) as well as its spatial derivatives, i.e. the forces.

A ‘weak cusp’ corresponds to $\gamma < 1$. In this case, the modulus of any component of the force generated by V_D goes to zero at the centre, reaches a maximum value at a certain distance from the centre, and then falls-off tending to zero at large distances by a Keplerian law. This behaviour of the force allows us to determine values of the parameters a , b , c , and M , for fixed γ , so as to create a system exhibiting a similar geometry and value of the total mass as the simplified system corresponding to the potential (4) of Section 2, the two systems being, hence, differentiated essentially

only by the presence of a central cusp as opposed to a harmonic core, respectively. The parameter determination is realized by the following algorithm:

(i) We set the ratios $a: b = \omega_y: \omega_x$ and $a: c = \omega_z: \omega_x$, where ω_x , ω_y , and ω_z are the parameters of (4).

(ii) We fix the value of a so that the quantity $\partial V_D / \partial x$ presents maximum at the point $(x = x_{\max}, y = 0, z = 0)$, with x_{\max} chosen so as to represent the point where the harmonic model in (4) yields a total mass equal to unity. We find $x_{\max} \simeq 1.06$.

(iii) We fix M so that the force F_x under the potential V_D be equal to the force F_x under the potential (4), with $m = 0$, at the point $(x = x_{\max}, y = 0, z = 0)$. Note that, since the value of the force depends essentially only on the total mass inside a given radius, this normalization means also that the total mass inside an ellipsoidal surface crossing $x = x_{\max}$ is nearly equal in the harmonic and in the γ -models.

We examine two values of γ in the weak cusp case, namely $\gamma = 0.3$ and 0.7 .

In the case, now, of a ‘strong cusp’ ($\gamma > 1$), criterion (ii) can no longer be implemented, since $\partial V_D / \partial x \rightarrow \infty$ as $x \rightarrow 0$ (with $y = z = 0$), implying that the quantity $\partial V_D / \partial x$ does not present any smooth maximum along any of the principal axes. As a simple (but somewhat arbitrary) way to bypass this difficulty, we keep a constant to the value $a = 6.67$ found by criterion (ii) in the second ‘weak cusp’ experiment ($\gamma = 0.7$). Then, we fix the remaining constants by criteria (i) and (iii). We run also two strong cusp experiments, with $\gamma = 1.3$ and 1.7 .

In all four experiments, the initial conditions are chosen as in Section 2, namely 200 initial points of zero velocity randomly distributed on equipotential surfaces with $V = E$, and E chosen uniformly in the range $0 \leq V \leq E_{\max}$, with E_{\max} chosen as $E_{\max} = V_D(x_{\max})$, so as to ensure that the resulting centrophilic orbits exhibit oscillations of amplitude at most equal to x_{\max} . However, here we integrate the orbits only up to $t = 1000$, since the complexity of force evaluation in the model V_D renders the computational cost of longer integration prohibitive. Yet, as shown below, our smallest found Lyapunov exponents are about $L \approx 10^{-2.5}$, implying that a time $t = 10^3$ is marginally greater than the saturation time $t \sim 1/L$ even for the orbits with smallest Lyapunov exponents.

Fig. 14 (analogous to Fig. 3, top row) shows the mean Lyapunov number $L = \bar{\chi}(t = 10^3)$ for our ensembles of orbits in the four above experiments, as a function of the central mass parameter m . We note immediately that power-law fittings are possible in only a range of values of m , i.e. above a critical threshold value $m > m_c(\gamma)$. In Fig. 14, an estimate of the threshold value is found by the abscissa of the points displayed by stars. They are computed as follows: the four inclined lines represent power-law fittings for the rightmost part of the numerical curve of L versus m in each experiment. The horizontal lines illustrate the level values of the quantity $L_0 = L(m = 0)$. We call L_0 the ‘residual Lyapunov exponent’. It represents the mean Lyapunov exponent of the centrophilic orbits when $m = 0$, i.e. under the influence of the central cusp only. The point at which a horizontal line of fixed L_0 intersects the corresponding inclined fitting line of L versus m in the same experiment (same γ) marks the position of a star-point, and the associated abscissa, i.e. a critical mass value m_c . From Fig. 14 it is straightforward to see that both L_0 and m_c increase in general with the strength of the cusp (i.e. the value of γ). On the other hand, it is clear from the numerical data points that an approximate power-law correlation between L and m persists, in all four experiments, for central mass parameters larger than $m = m_c$. A physical understanding of this

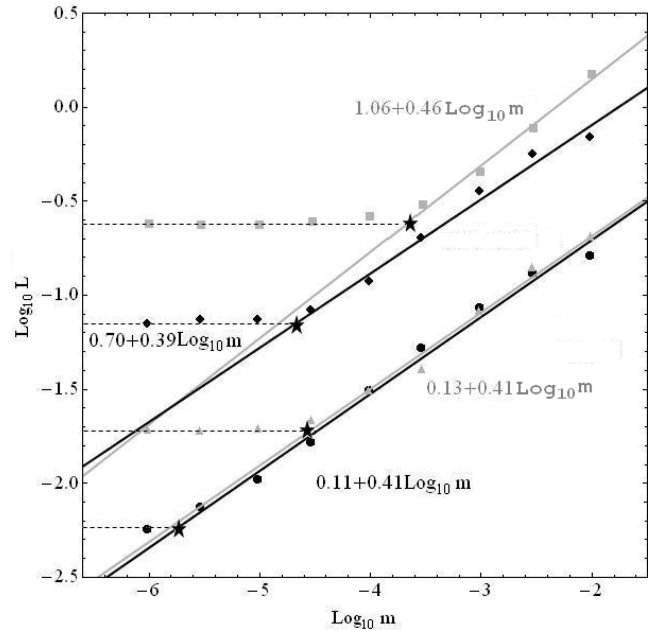


Figure 14. The mean Lyapunov exponent versus the central mass parameter m in four Dehnen triaxial models with central cusps (see text). Black filled circles correspond to the data points for the cusp exponent $\gamma = 0.3$, grey triangles to $\gamma = 0.7$, black rhombuses to $\gamma = 1.3$, and grey squares to $\gamma = 1.7$. The straight lines (black or grey) are power-law fittings obtained by the rightmost seven points for $\gamma = 0.3$, five points for $\gamma = 0.7$, five points for $\gamma = 1.3$, and four points for $\gamma = 1.7$. The horizontal dashed lines correspond to the values $\log_{10} L_0$, where L_0 is the ‘residual Lyapunov exponent’ in each case (see text). The points where each horizontal line intersects the fitting line for the same corresponding γ are marked as stars.

phenomenon is the following: the chaotic scattering caused by the cusp itself acts dynamically as a central mass concentration, whose distribution is not point-like but follows the cusp density law. As long as the BH mass is small, the effect of the cusp is dominant over the effect of the BH. Thus, the mean Lyapunov exponent of the centrophilic orbits remains nearly equal to the residual Lyapunov exponent L_0 . But beyond the BH mass scale $m = m_c$, the BH dominates over the central cusp. Then, we recover a correlation of L with m . This goes asymptotically to an effective power law. Furthermore, the exponents found by fitting in the range $m > m_c$ are all about $p \simeq 0.4$, i.e. not very different from those of the corresponding data in Fig. 3, the essential difference in the two plots being with respect to whether or not we observe a critical mass scale in which the power-law breaks.

We note finally, that despite the sparsity of their data points, the results of Merritt & Valluri (1996), reproduced here as Fig. 4(b), show essentially the same structure as the results of Fig. 14. Thus, the residual chaos phenomenon explains the plateau of the curve L versus m in the data of Merritt & Valluri (1996) as well.

5 THE $L \propto m^p$ LAW IN DISC-BARRED GALAXIES

N -body simulations of barred galaxies (e.g., Friedli & Benz 1993; Friedli 1994; Norman et al. 1996) have demonstrated that the growth of a central mass concentration induces secular evolution in such systems as well. In fact, although dynamically not favoured, BH growth to a mass level as high as 10^8 – $10^9 M_\odot$, corresponding to a few per cent of the mass of a typical galactic bar, could induce even a total destruction of the bar, with its conversion into a nearly

axisymmetric bulge-like component. Test particle integrations in barred potentials (Pfenniger 1984; Pfenniger & de Zeeuw 1989; Hasan et al. 1993; Norman et al. 1996; Shen & Sellwood 2004) indicate that a primary mechanism responsible for the secular evolution of bars, and even bar dissolution, is chaos induced by the central mass.

Hereafter we study the dependence of Lyapunov exponents on the central mass parameter in rotating disc-barred galaxies. Two points should be immediately emphasized. (i) Our modelling in previous sections was based on the existence of box-like centrophilic chaotic orbits. Such orbits cannot exist in rotating disc-barred galaxies. However, as shown in the sequel, centrophilic orbits appear around the main families of planar periodic orbits (e.g., the x_1 family). Note that the presence of some type of centrophilic orbits is an indispensable feature of bars with a rising density profile in the centre. As discussed below, albeit different in morphology, the centrophilic orbits in barred galaxies are found numerically to exhibit a similar chaotic behaviour as the boxy centrophilic orbits in elliptical galaxies. (ii) Besides the central mass, chaos is generated by the interaction of resonances in the corotation domain (Contopoulos 1981; Pfenniger 1984; Sparke & Sellwood 1987; Pfenniger & Friedli 1991; Kaufmann & Contopoulos 1996; Patsis et al. 1997; Fux 2001; Pichardo, Martos & Moreno 2004; Kaufmann & Patsis 2005). Nevertheless, this type of chaos is a quite distinct phenomenon. In fact, most chaotic orbits in the corotation domain belong to the so-called hot population (Sparke & Sellwood 1987), hence they are not centrophilic.

5.1 Potential model

As a case study, we employ the barred-galaxy potential introduced by Kaufmann & Contopoulos (1996) in a rough self-consistent modelling of the galaxy NGC3992. Adding a component for the central mass, the total potential is analysed as

$$V_{\text{tot}} = V_{\text{bh}} + V_{\text{h}} + V_{\text{d}} + V_{\text{b}} \quad (33)$$

where V_{bh} is the potential generated from the central mass (BH), while V_{h} , V_{d} , V_{b} are dark halo, disc, and bar potential components, respectively. The potential of the central mass is, as before,

$$V_{\text{bh}} = -\frac{m_{\text{bh}}}{\sqrt{r^2 + d^2}}. \quad (34)$$

The remaining terms are as in Kaufmann & Contopoulos (1996). The dark halo term is

$$V_{\text{h}}(r) = \frac{-M_{\text{h}}}{\sqrt{r^2 + b_{\text{h}}^2}}. \quad (35)$$

The disc term corresponds to an exponential disc:

$$V_{\text{d}}(r) = -\Sigma_0 \pi r \left[I_0 \left(\frac{1}{2} \epsilon_{\text{d}} r \right) K_1 \left(\frac{1}{2} \epsilon_{\text{d}} r \right) - I_1 \left(\frac{1}{2} \epsilon_{\text{d}} r \right) K_0 \left(\frac{1}{2} \epsilon_{\text{d}} r \right) \right], \quad (36)$$

where I_0 , I_1 and K_0 , K_1 are modified Bessel functions of the first and second kind, respectively. The bar term is of the Ferrers $n = 2$ type, with the major axis aligned with the y -axis:

$$V_{\text{b}}(x, y, z) = -\frac{105 M_{\text{b}}}{96} \left[3 (2 W_{110} x^2 y^2 - W_{120} x^4 y^2 - W_{210} x^2 y^2 - W_{100} y^2 + W_{020} x^4 + W_{200} y^4 - W_{010} x^2) + W_{000} - W_{030} x^6 - W_{300} y^6 \right], \quad (37)$$

Table 1. Parameters of the disc-barred galactic potential. The units are kpc^{-1} for ϵ_{d} , kpc for a , b , c and b_{h} , $10^{10} M_{\odot}$ for M_{h} , M_{b} , m_{bh} , $\text{kms}^{-1} \text{kpc}^{-1}$ for Ω_{p} , $M_{\odot} \text{pc}^{-2}$ for Σ_0 .

Bar:	M_{b}	α	b	c	Ω_{p}
	1.5	5.5	2.1	0.55	43.6
Disc:	Σ_0	ϵ_{d}			
	750	0.235			
Halo:	M_{h}	b_{h}			
	27.5	12			

where the coefficients W_{ijk} are given by elliptic integrals. All model's parameters, as well as the value of the pattern speed Ω_{p} are as in Kaufmann & Contopoulos (1996), referring to the model for the galaxy NGC3992. They are summarized in Table 1. Note that the original model contains also a spiral-arm term, which, however, is only important at radii beyond the end of the bar, and it is here ignored.

5.2 Numerical experiments

As in Section 2, we numerically integrate the equations of motion, as well as the variational equations, for planar orbits under the Hamiltonian (in cylindrical coordinates)

$$H(r, \theta, p_r, p_{\theta}) = \frac{1}{2} \left(p_r^2 + \frac{p_{\theta}^2}{r^2} \right) - \Omega_{\text{p}} p_{\theta} + V(r, \theta) = E_j, \quad (38)$$

where E_j is the Jacobi constant. The Hamiltonian (38) describes the motion in a rotating frame with pattern speed Ω_{p} , while p_{θ} is the angular momentum in the inertial frame of reference.

Initial conditions are chosen in a way so as to ensure that they give rise to centrophilic orbits. To this end, we consider, as above, ensembles of 200 orbits with initial positions uniformly distributed on a cycle of radius $r = 0.1$ around the galactic centre. Initial velocities are given in the direction radially outwards, with modulus chosen so that the value of the Jacobi constant is uniformly distributed in the range $-2.16 \times 10^5 \leq E_j \leq -2.03 \times 10^5$. This range is chosen so as to correspond to energies well below the value at the Lagrangian equilibrium point L_1 , i.e. $E_{j,1} = -1.915 \times 10^5$. The corresponding orbits lie then always inside the corotation domain, i.e. they support the bar. Orbit ensemble integrations are done for a time $t = 10^5$ (in comparison, orbital periods are of order ~ 0.1). In different experiments the central mass varies in the range $10^{-6} \leq m \leq 10^{-2}$. Fig. 15 shows the main result: the mean Lyapunov number L of the chaotic orbits chosen as above is plotted against the mass parameter m , chosen here as the ratio $m = m_{\text{bh}}/m_{\text{bar}}$, since this ratio is relevant to a quantification of the rate of secular evolution of the bar. We observe again that the numerical data can be fitted by a power law $L \propto m^p$, with $p = 0.51$.

We now interpret the mechanisms of chaos and identify the families of orbits which are responsible for this behaviour.

5.3 Interpretation

The mechanism by which a central BH generates chaos in a disc-barred galaxy can be visualized with the help of phase portraits, obtained by means of a suitable surface of section. Here we employ the *apocentric* condition $\dot{r} = 0, \ddot{r} < 0$, in order to define the surface

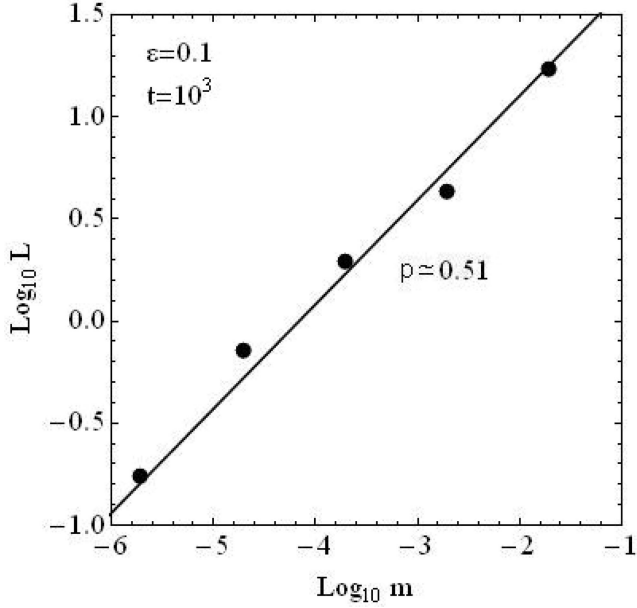


Figure 15. Logarithm of the mean Lyapunov number of the orbits in the ensembles of initial conditions as described in the text versus the central mass parameter $m = m_{\text{bh}}/m_{\text{bar}}$ (in logarithmic scale) in a disc-barred galaxy model. The logarithmic slope indicates a power-law exponent $p = 0.51$.

of section. We then plot the intersection points of all orbits with the above section as projected on the plane (θ, p_θ) .

Fig. 16 shows the surface of section portrait at the energies (Jacobi constant values) $E_j = -204\,000$ and $-195\,000$, without central BH (Figs 16a and d), or with a BH of mass $m_{\text{bh}} = 10^6 M_\odot$ (Figs 16b and e). The change of phase space structure is evident, namely the insertion of the central mass destroys many rotational Kolmogorov – Arnold – Moser (KAM) curves, corresponding to regular (quasi-periodic) orbits around the galactic centre. Also, at the second energy level (lower panels), which corresponds to motion closer to corotation, a number of librational KAM curves around the 1:4 island of stability are destroyed. In fact, one can see that at both energy levels the orbits converted to chaotic are *tube* orbits around the 2:1 and 4:1 branches of the x_1 stable periodic orbit. The periodic orbits themselves at the corresponding energies are shown in Figs 16(c) and (f), respectively. The 2:1 orbits exist up to energies $\approx -199\,000$. When $m_{\text{bh}} = 0$, the quasi-periodic tube orbits around a 2:1 orbit give rise to two islands of stability in the surface of section. The outermost librational invariant curves of these islands correspond to thick tube orbits (Fig. 17). The crucial difference between the two tube orbits in Figs 17(a) and (b) is that in Fig. 17(a) the tube orbit leaves a hole in the centre, whose dimension is larger than the BH’s sphere of influence. On the contrary, the tube thickness of the orbit in Fig. 17(b) is larger than the half-width of the orbit’s amplitude of oscillation in the y -axis, i.e. the orbits leaves no hole in the centre. Then, after the insertion of the central mass, the orbit with same initial conditions as in Fig. 17(a) retains its regular (quasi-periodic) character (Fig. 17c), while the orbit with same

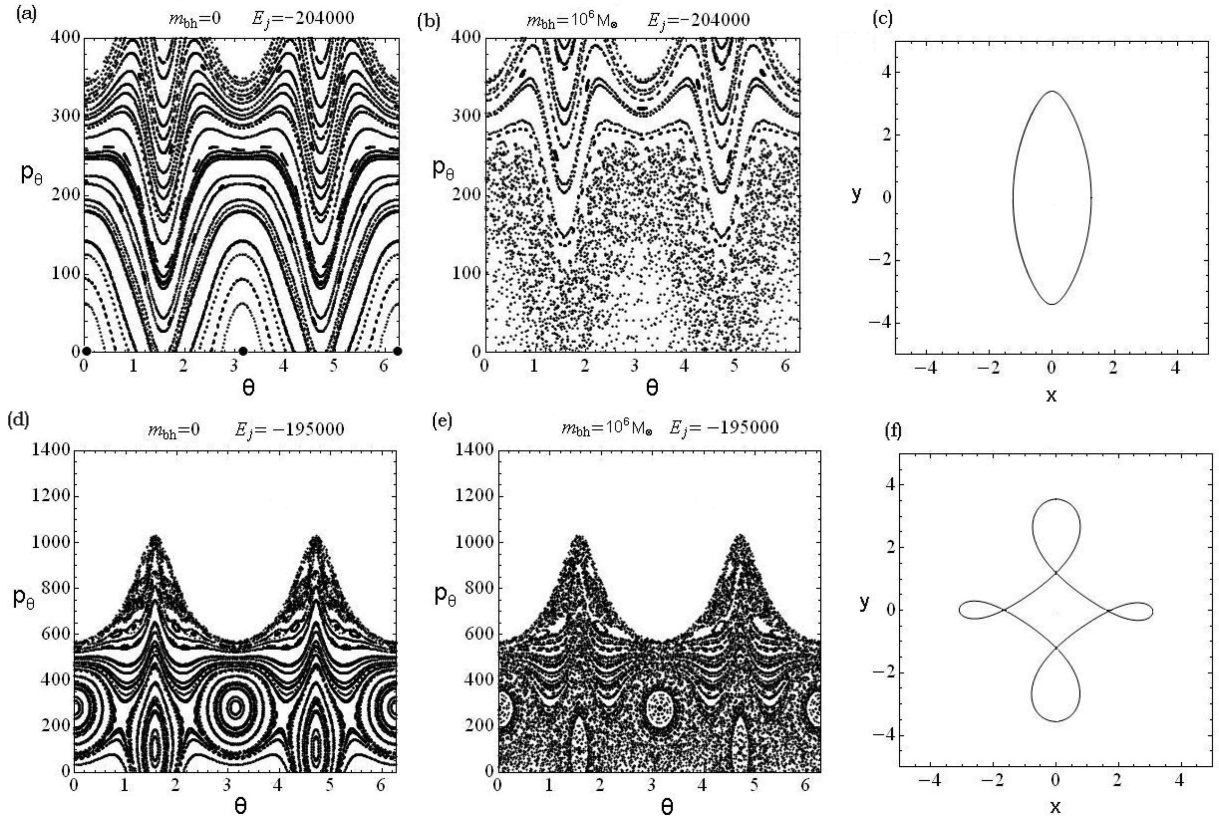


Figure 16. Apocentric Poincaré surfaces of section with $m_{\text{bh}} = 0$ at the energies (a) $E_j = -204\,000$ and (d) $E_j = -195\,000$. (b and e) Same as in (a and d), but now with a central BH of mass $m_{\text{bh}} = 10^6 M_\odot$. The x_1 periodic orbit (c) at the energy $E_j = -204\,000$ has a 2:1 form (two apocentric passages per revolution in the rotating frame), while (f) at the energy $E_j = -195\,000$ it has a 4:1 form.

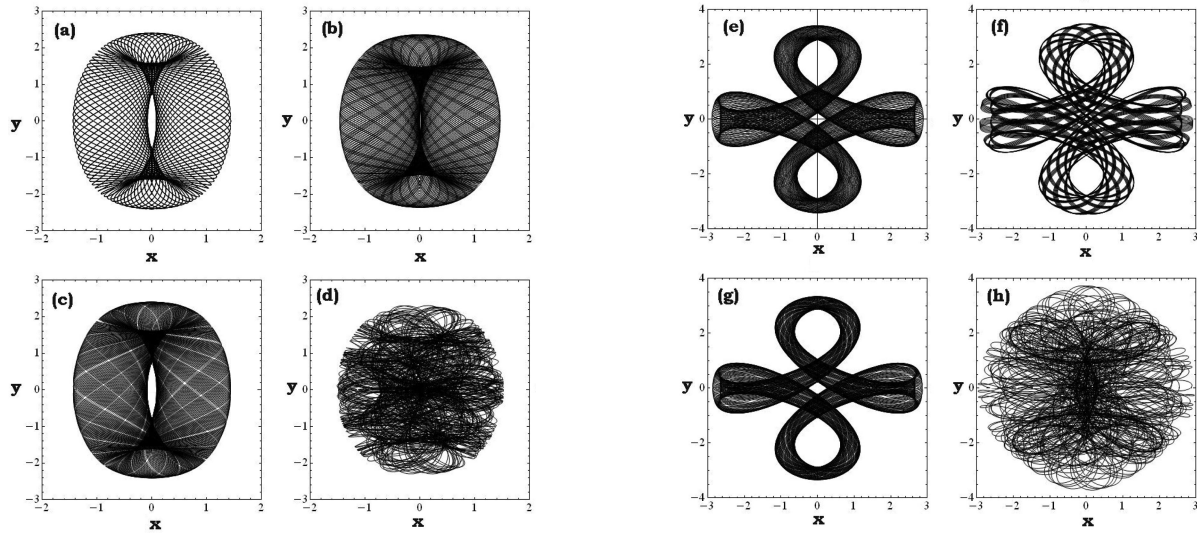


Figure 17. (a) Tube orbit with energy $-216\,000$ around the 2:1 periodic orbit before the insertion of the central mass. The initial conditions correspond to a librational invariant curve of the 2:1 island of stability which survives after the insertion of the BH. (b) Same as in (a), but for initial conditions on an invariant curve of the 2:1 island of stability which is destroyed after the insertion of the BH. (c) The orbit with same initial conditions as in (a) remains ordered after the insertion of a central mass $m_{\text{bh}} = 10^6 M_{\odot}$. (d) On the contrary, the orbit with same initial conditions as in (b) is converted to chaotic. (e and f) Same as in (a and b) but for two tube orbits of the 4:1 resonance. (g and h) The orbits with the same initial conditions as in (e and f), respectively, after the insertion of the central mass $m_{\text{bh}} = 10^6 M_{\odot}$. The one of (g) remains regular, while the one of (h) is chaotic.

initial conditions as in Fig. 17(c) becomes chaotic (Fig. 17d). A similar criterion applies to whether or not a thick tube orbit around the 4:1 periodic orbit becomes regular or chaotic after the insertion of the central mass (Figs 17e–h). In fact, one readily finds that the initial conditions separating these two types of orbits correspond to the last librational KAM curve in the 4:1 island of stability of the section of Fig. 16(d).

Investigating the efficiency of the above mechanism to other resonances, one finds that the mechanism is not able to produce chaotic orbits in the cases of other low-order resonances like 3:1 and 6:1. In fact, the tube orbits trapped around these central periodic orbits in this model form rather small islands of stability. Thus, the tube thickness is small, and we find no tube orbits able to cross the central masses’ sphere of influence. A similar restriction holds for higher order families in the same model.

6 CONCLUSIONS

In this paper we analyse the origin of a numerically observed approximate power-law relation $L \propto m^p$, with $p \sim 0.3\text{--}0.5$, where L is the mean Lyapunov exponent of centrophilic orbits in galaxies with central masses (BHs), and m the mass parameter, i.e. the ratio of the central mass over the mass of the galaxy. Also, we find that such a law can be recovered in quite different contexts and models of galactic systems, ranging from elliptical galaxies with cores or cusps to rotating barred galaxies. In particular:

(i) We first make numerical experiments with a simple model of elliptical galaxy with smooth central force field, to which the force field of the central mass is superposed. The experiments confirm the power law $L \propto m^p$, when L is estimated through its ‘finite-time’ analogue, i.e. the mean value of finite-time Lyapunov exponents. We demonstrate the statistics of these values for centrophilic orbits. We also find that p has a tendency towards the upper limit 0.5 at longer integration times.

(ii) We demonstrate that the law $L \propto m^p$ can be extracted also from compiling data of previous works in the literature (Merritt & Valluri 1996; Kandrup & Sideris 2002), in galaxies with both smooth and cuspy centres.

(iii) We make a theoretical analysis of the Lyapunov exponents for centrophilic box-like orbits in elliptical galaxies. We demonstrate that the mean Lyapunov exponent can be obtained by independently estimating (a) the mean value of the so-called stretching number (=one-step Lyapunov number) at every transit of an orbit from the sphere of influence of the central mass, and (b) the rate of visits of the orbits to the sphere of influence. In both cases, we find how the various estimates depend on m as well as on the orbital energy. Regarding (b), we find two different estimates, according to whether an orbit can be characterized as ‘planar’ or ‘3D’. Putting all estimates together, one arrives at a theoretical reproduction of the $L \propto m^p$ law.

(iv) In the case of models with central cusps, we find a critical mass scale m_c , such that for central mass parameters $m < m_c$ the chaotic behaviour of the centrophilic orbits is dominated by the central cusp (we call this ‘residual chaos’), while for $m > m_c$ an approximate power-law correlation $L \propto m^p$ is restored, with $p \approx 0.4$. The critical mass scale m_c as well as the ‘residual mean Lyapunov exponent’ L_0 are increasing functions of the exponent γ in power-law central cusps $\rho(r) \sim r^{-\gamma}$.

(v) We finally explore numerically the correlation between L and m for the centrophilic orbits in disc galaxies with rotating bars. In this case, while there can be no box-like centrophilic orbits, we find several quasi-periodic tube orbits around the main families of periodic orbits (like 2:1 or 4:1), for which the tube is thick enough so as to pass arbitrarily close to the centre. These orbits support the rising density profile of the bar at the centre. Their initial conditions are close to the last librational KAM curve of the islands of stability around their corresponding periodic orbits. Numerically, we observe that only the tube orbits around the lowest-order periodic orbits can become centrophilic. Furthermore, for the chaotic counterparts of

these orbits, after the insertion of the BH, we numerically recover again a correlation of the form $L \propto m^p$.

ACKNOWLEDGEMENTS

This research is supported by the Research Committee of the Academy of Athens (grant 200/815). ND was supported by the State Scholarship Foundation of Greece (IKY).

REFERENCES

- Binney J., Merrifield S., 1998, *Galactic Astronomy*. Princeton Univ. Press, Princeton, NJ
- Binney J., Tremaine S., 2008, *Galactic Dynamics*, 2nd edn. Princeton Univ. Press, Princeton, NJ
- Contopoulos G., 1960, *Z. Astrophys.*, 49, 273
- Contopoulos G., 1981, *A&A*, 102, 265
- Contopoulos G., Voglis N., Kalapotharakos C., 2002, *Celest. Mech. Dyn. Astron.*, 83, 191
- Debattista V. P., 2006, in Kannappan S. J., Redfield S., Kessler-Silacci J. E., Landraiu M., Drory N., eds, *ASP Conf. Ser. Vol. 352, New Horizons in Astronomy: Frank N. Bash Symposium 2005*. Astron. Soc. Pac., San Francisco, p. 161
- Dehnen W., 1993, *MNRAS*, 265, 250.
- Eftymiopoulos C., Contopoulos G., Giorgilli A., 2004, *J. Phys. A: Math. Gen.*, 37, 10831.
- Eftymiopoulos C., Voglis N., Kalapotharakos C., 2007, *Lecture Notes Phys.*, 729, 297
- Faber S. M. et al., 1997, *AJ*, 114, 1771
- Ferrarese L., Ford H. C., 2005, *Space Sci. Rev.*, 116, 523
- Ferrarese L., van den Bosch F. C., Ford H. C., Jaffe W., O’Connell R. W., 1994, *AJ*, 108, 1598
- Fridman T., Merritt D., 1997, *AJ*, 114, 1479
- Friedli D., 1994, in Shlosman I., ed., *Mass-Transfer Induced Activity in Galaxies*. Cambridge Univ. Press, Cambridge, p. 268
- Friedli D., Benz W., 1993, *A&A*, 268, 65
- Froeschlé C., Lega E., Gonczi R., 1997, *Celest. Mech. Dyn. Astron.*, 67, 41
- Fux R., 2001, *A&A*, 373, 511
- Gebhardt K. et al., 1996, *AJ*, 112, 105
- Gebhardt K. et al., 2000, *AJ*, 119, 1157
- Gerhard O. E., Binney J., 1985, *MNRAS*, 216, 467
- Gültekin K. et al., 2009, *ApJ*, 695, 1577
- Gültekin K. et al., 2009, *ApJ*, 698, 198
- Hasan H., Pfenniger D., Norman C., 1993, *ApJ*, 409, 91
- Holley-Bockelmann K., Mihos J. C., Sigurdsson S., Hernquist L., 2001, *ApJ*, 549, 149
- Holley-Bockelmann K., Mihos J. C., Sigurdsson S., Hernquist L., Norman C., 2002, *ApJ*, 567, 817
- Jesseit R., Naab T., Burkert A., 2005, *MNRAS*, 360, 1185
- Kalapotharakos C., 2008, *MNRAS*, 389, 1709
- Kalapotharakos C., Voglis N., 2005, *Celest. Mech. Dyn. Astron.*, 92, 157
- Kalapotharakos C., Voglis N., Contopoulos G., 2004, *A&A*, 428, 905
- Kandrup H., Sideris I., 2002, *ApJ*, 471, 82
- Kaufmann D. E., Contopoulos G., 1996, *A&A*, 309, 381
- Kaufmann D. E., Patsis P., 2005, *ApJ*, 624, 693
- Kormendy J., Ho L. C., 2013, *Annu. Rev. Astron. Astrophys.*, 51, 511
- Kormendy J., Richstone D., 1995, *Annu. Rev. Astron. Astrophys.*, 33, 581
- Kormendy J. et al., 1997, *ApJ*, 482, L139
- Kormendy J., Bender R., Evans A. S., Richstone D., 1998, *AJ*, 115, 1823
- Lauer T. R. et al., 1995, *AJ*, 110, 2622
- McConnell N. J., Ma C. P., 2013, *ApJ*, 764, 184.
- Merritt D., 1999, in Merritt D. R., Valluri M., Sellwood J. A., eds, *ASP Conf. Ser. Vol. 182, Galaxy Dynamics*. Astron. Soc. Pac., San Francisco, p. 164
- Merritt D., 2013, *Dynamics and Evolution of Galactic Nuclei*. Princeton Univ. Press, Princeton, NJ
- Merritt D., Fridman T., 1996, *ApJ*, 460, 136
- Merritt D., Quinlan D., 1998, *ApJ*, 498, 625
- Merritt D., Valluri M., 1996, *ApJ*, 471, 82
- Merritt D., Valluri M., 1999, *AJ*, 118, 1177
- Merritt D., Vasiliev E., 2011, *ApJ*, 726, 61
- Miralda-Escudé J., Schwarzschild M., 1989, *ApJ*, 339, 752.
- Muzzio J. C., 2006, *Celest. Mech. Dyn. Astron.*, 96, 85
- Muzzio J. C., Carpintero D., Wachlin F. C., 2005, *Celest. Mech. Dyn. Astron.*, 91, 173
- Norman C. A., Sellwood J. A., Hasan H., 1996, *ApJ*, 462, 114
- Patsis P. A., Eftymiopoulos C., Contopoulos G., Voglis N., 1997, *A&A*, 326, 493
- Pfenniger D., 1984, *A&A*, 134, 373
- Pfenniger D., de Zeeuw T., 1989, in Merritt D., ed., *Dynamics of Dense Stellar Systems*. Cambridge Univ. Press, Cambridge, p. 81
- Pfenniger D., Friedli D., 1991, *A&A*, 252, 75
- Pichardo B., Martos M., Moreno E., 2004, *ApJ*, 609, 144
- Shen J., Sellwood J. A., 2004, *ApJ*, 604, 614
- Sparke L. S., Sellwood J. A., 1987, *MNRAS*, 225, 653
- Valluri M., Debattista V. P., Quinn T., Moore B., 2010, *MNRAS*, 403, 525
- van der Marel R. P., de Zeeuw P. T., Rix H. W., 1997, *ApJ*, 488, 119
- Vasiliev E., Athanassoula E., 2012, *MNRAS*, 419, 3268.
- Voglis N., Contopoulos G., 1994, *J. Phys. A: Math. Gen.*, 27, 4899
- Young P. J., 1977, *ApJ*, 217, 287
- Young P. J., 1980, *ApJ*, 242, 1232

APPENDIX A:

We theoretically estimate the local value of the ‘stretching number’ of an orbit transiting the sphere of influence of the central mass (Fig. A1), schematic, as follows: approximating the motion during the transit as Keplerian, in polar coordinates (r, ϕ) with respect to

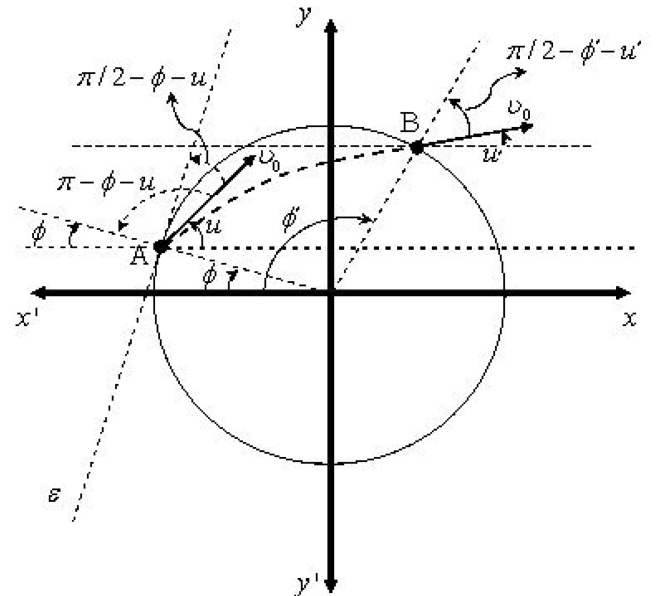


Figure A1. Schematic representation of our model for orbit transits via the sphere of influence of the central mass. An orbit enters the sphere at point A and exits at point B. Hyperbolic Keplerian dynamics is assumed in order to estimate the orbit’s local ‘stretching number’ arising at the transit (see text).

the origin on a plane including the origin and the entry and exit points (A,B, respectively), one has

$$\frac{1}{r} = \frac{Gm}{C^2} + A \cos(\phi - \phi_0), \quad (\text{A1})$$

where C is the local value of the angular momentum (assumed constant during the transit, see Section 3). The constant A is given by

$$A = e \frac{Gm}{C^2}, \quad (\text{A2})$$

where $e = \sqrt{1 + 2EC^2/mG^2}$, whereas ϕ_0 is the angle corresponding to the closest approach to the origin, at distance r_{\min} . The orbit has the same velocity measure v_0 at the points A and B. We assume that the velocity vector at A forms an angle u with the horizontal axis.

With the above conventions, to a given entry angle ϕ corresponds a given exit angle ϕ' from the sphere of influence. After some algebra (taking into account equation A1 as well as the preservation of energy and angular momentum), we find

$$\phi - \phi' = 2 \cos^{-1} \left[\frac{v_0 \sin(\phi + u)}{\sqrt{(Gm/r_m v_0 \sin(\phi + u))^2 + v_0^2 - 2Gm/r_m}} \right] \times \left(1 - \frac{Gm}{r_m v_0^2 \sin^2(\phi + u)} \right). \quad (\text{A3})$$

The local value of the stretching number can now be estimated by the difference in ϕ' for two nearby orbits entering at slightly different angles ϕ . Taking the derivative of equation (A3) we have

$$\left| \frac{d\phi'}{d\phi} \right| = \left| 1 + \frac{d}{d\phi} \left[2 \cos^{-1} \left[\frac{v_0 \sin(\phi + u)}{\sqrt{(Gm/r_m v_0 \sin(\phi + u))^2 + v_0^2 - 2Gm/r_m}} \right] \left(1 - \frac{Gm}{r_m v_0^2 \sin^2(\phi + u)} \right) \right] \right|. \quad (\text{A4})$$

Re-orienting the frame of reference, without loss of generality the parameter u can be set equal to zero. The quantity $|d\phi'/d\phi|$ is the measure of the stretching number a for the transit motion inside the sphere r_m . One can check that for typical energies of centrophilic orbits, one has $2mr_m v_0^2 \ll r_m^2 v_0^4$. Then, equation (A4) reduces to

$$\left| \frac{d\phi'}{d\phi} \right| \simeq \left| 1 - 2 \frac{1 + m \csc^2 \phi / r_m v_0^2}{1 + m^2 \csc^2 \phi / r_m^2 v_0^4} \right|. \quad (\text{A5})$$

The mean stretching number of a transit at given velocity v_0 , with respect to all possible angles ϕ can be estimated by the integral of

the quantity $\log |d\phi'/d\phi|$ over all possible angles:

$$\begin{aligned} \overline{\log \left| \frac{d\phi'}{d\phi} \right|} &= \frac{2}{\pi} \int_0^{\pi/2} \log \left| \frac{d\phi'}{d\phi} \right| d\phi \\ &= \frac{2}{\pi} \int_0^{\pi/2} \log \left| 1 - 2 \frac{1 + \frac{m}{r_m v_0^2} \csc^2 \phi}{1 + \frac{m}{r_m^2 v_0^4} \csc^2 \phi} \right| d\phi \\ &= \frac{2}{\pi} \int_0^{\pi/2} \log \left| \left(1 - 2 \frac{\alpha_0 + \sin^2 \phi}{\alpha_0^2 + \sin^2 \phi} \right) \right| d\phi \\ &= \frac{2}{\pi} \int_0^{\pi/2} \log \left(2 \frac{\alpha_0 + \sin^2 \phi}{\alpha_0^2 + \sin^2 \phi} - 1 \right) d\phi \\ &= \log \left(2 \frac{1 + \alpha_0}{1 + \alpha_0^2} - 1 \right) \\ &\quad + 2 \log \frac{\sqrt{1 + \alpha_0^2} \left(1 + \sqrt{\frac{\alpha_0(\alpha_0 - 2)}{\alpha_0^2 - 2\alpha_0 - 1}} \right)}{\alpha_0 + \sqrt{1 + \alpha_0^2}}, \end{aligned} \quad (\text{A6})$$

where $\alpha_0 = m/r_m v_0^2$. At mass ranges $10^{-5} < m < 10^{-2}$ the value of α_0 is in general a small quantity, except for small energies ($E < 0.03$ in our units), which, however, can be readily checked to correspond to orbits residing always within the sphere $r = r_m$, i.e. pyramids (Merritt & Vasiliev 2011). Excluding such orbits, we set $\alpha_0 = 0$ in the previous equation and obtain

$$\begin{aligned} \overline{\log \left| \frac{d\phi'}{d\phi} \right|} &\simeq \log(1 + 2\alpha_0) + 2 \log \frac{\left(1 + \sqrt{\frac{-2\alpha_0}{-2\alpha_0 - 1}} \right)}{a + 1} \\ &= \log(1 + 2\alpha_0) + 2 \log \frac{\left(1 + \sqrt{\alpha_0} \sqrt{\frac{-2}{-2\alpha_0 - 1}} \right)}{a + 1}. \end{aligned} \quad (\text{A7})$$

Expanding equation (A7) with respect $a_0^{1/2}$ we find

$$\begin{aligned} \overline{\log \left| \frac{d\phi'}{d\phi} \right|} &\simeq 2\alpha_0 + 2 \log(1 + \sqrt{\alpha_0} \sqrt{2}) = 2\alpha_0 + 2\sqrt{2} \sqrt{\alpha_0} \\ &= \frac{2}{(r_m v_0^2)} m + \frac{\sqrt{22}}{(r_m v_0^2)^{1/2}} \sqrt{m} \simeq \sqrt{\frac{8}{(r_m v_0^2)}} \sqrt{m}. \end{aligned} \quad (\text{A8})$$

In equation (A8) the quantity r_m depends on m ($r_m \propto m^{1/3}$). Furthermore in the limit of the sphere of BH's influence, energy is approximately equal with the kinetic energy ($v_0^2 \propto E$), whereby the last expression can be written in the form

$$\bar{a} \approx \overline{\log \left| \frac{d\phi'}{d\phi} \right|} \propto \frac{m^{1/3}}{E^{1/2}}, \quad (\text{A9})$$

i.e. we arrive at the estimate of equation (17).

This paper has been typeset from a $\text{\TeX}/\text{\LaTeX}$ file prepared by the author.